Princeton Plasma Physics Laboratory

PPPL- 4391

PPPL- 4391

Comparisons of Predicted Plasma Performance in ITER H-mode Plasmas with Various Mixes of External Heating

R.V. Budny

Revised April 2009

Prepared for the U.S. Department of Energy under Contract DE-AC02-76CH03073.

Princeton Plasma Physics Laboratory
Report Disclaimers

Full Legal Disclaimer

Trademark Disclaimer

PPPL Report Availability

Princeton Plasma Physics Laboratory:

http://www.pppl.gov/techreports.cfm

Office of Scientific and Technical Information (OSTI):

http://www.osti.gov/bridge

Related Links:

U.S. Department of Energy

Office of Scientific and Technical Information

Fusion Links

Comparisons of predicted plasma performance in ITER H-mode plasmas with various mixes of external heating

R.V. Budny*
Princeton Plasma Physics Laboratory, Princeton, NJ 08543
(Dated: May 28, 2009)

Performance in H-mode DT plasmas in ITER with various choices of heating systems are predicted and compared. Combinations of external heating by Negative Ion Neutral Beam Injection (NNBI), Ion Cyclotron Range of Frequencies (ICRF), and Electron Cyclotron Heating (ECRH) are assumed. Scans with a range of physics assumptions about boundary temperatures in the edge pedestal, alpha ash transport, and toroidal momentum transport are used to indicate effects of uncertainties. Time-dependent integrated modeling with the PTRANSP code is used to predict profiles of heating, beam torque, and plasma profiles. The GLF23 model is used to predict temperature profiles. Either GLF23 or the assumption of a constant ratio for χ_ϕ/χ_i is used to predict toroidal rotation profiles driven by the beam torques. Large differences for the core temperatures are predicted with different mixes of the external heating during the density and current ramp-up phase, but the profiles are similar during the flattop phase. With $\chi_\phi/\chi_i = 0.5$, the predicted toroidal rotation is relatively slow and the flow shear implied by the pressure, toroidal rotation, and neoclassical poloidal rotation are not sufficient to cause significant changes in the energy transport or steady state temperature profiles. The GLF23-predicted toroidal rotation is faster by a factor of six, and significant flow shear effects are predicted. Heating mixes with more NNBI power are predicted to have up to 20% higher fusion power during steady state phases. This advantage is decisive in some cases where the physics assumptions are close to marginal or critical values. L-mode plasmas are predicted having $Q_{\rm DT} \simeq$ 2-4.

PACS numbers: 07.05.Tp, 28.52.-s, 28.52.Av, 28.52.Cx

1. Introduction

The heating systems for ITER plasmas are being designed. The purpose of this paper is to compare the plasma performance predicted with alternative choices of the heating. The external heating systems considered are: Negative ion Neutral Beam Injection (NNBI), Ion Cyclotron Resonance Heating (ICRH), and Electron Cyclotron Resonance Heating (ECRH). The standard heating modes considered for initial DT operation are D-NNBI at 1MeV from two beam lines delivering 16.5 MW each; ICRH with ^{3}He minority at 53 MHz delivering up to 20 MW; and ECRH in O-mode at 170 GHz delivering up to 20 MW. Alternative plans for later upgrades and possibly even for initial DT operation (besides the two NNBI and ICRH systems) are for zero, one, or three beam-lines, up to 60 MW ECRH, and up to 20 MW lower hybrid current drive.

This paper uses the PTRANSP code [1, 2] to generate self-consistent, time-dependent integrated predictions of H-mode DT plasmas. It extends Ref. [1] to include ECRH, systematic scans of the external heating, and an additional variety of physics assumptions. A range of assumptions about boundary temperatures in the edge pedestal, and about alpha ash transport are used to indicate effects of some of the uncertainties in the physics that affects plasma performance.

2. External Heating

ITER is being constructed to study physics and technological issues for the development of fusion reactors. Among the goals [3] are the production of 400 MW of fusion energy $P_{\rm DT}$ for long durations (300-500 s), and of fusion gain $Q_{\rm DT} \equiv P_{\rm DT}/P_{\rm ext} = 10$. Here $P_{\rm ext}$ is the main external heating power, planned to be at most 73 MW. These conditions should facilitate studies of alpha heating in near-burning plasma. The Ohmic heating, expected to be $\simeq$ 1-2 MW is conventionally not counted in $P_{\rm ext}$. Also power that might be required for control of MHD stability is not included.

Five mixes of heating (with associated current and torque drives, and fueling) are assumed to examine various possibilities and contingencies for ITER. These are indicated in Table I, and include zero, one, two, or three beam lines, up to 20 MW ICRH, and various amounts of ECRH power. The assumed time evolutions of the heating powers are shown in Fig. 1. The $P_{\rm ext}$ is assumed to start with 73 MW during the density and I_p ramp-up, and this is assumed to be sufficient to cause the LH transition. The total is later stepped down to explore steady state conditions with decreased $P_{\rm ext}$. The alpha heating could compensate to a degree for the reduced $P_{\rm ext}$ and might be able to maintain relatively high $P_{\rm DT}$ and increased $Q_{\rm DT}$. In some scans, even ignition ($Q_{\rm DT} \simeq \infty$) is predicted.

The NNBI voltage is assumed to be 1 MeV. The 3-D geometry of the sources, aiming angles, and beam ducts

with a small footprint in the plasma and with below-axis aiming is assumed [1]. The average height of the D^0 trajectories at the location of minimum major radius is 30 cm below the vacuum vessel midplane. The plasma center is 52-53 cm above the midplane. Examples of D^0 beam trajectories are shown in Fig. 2.

The ICRH is assumed to use ^{3}He as the minority ion species. The frequency is fixed at 52.5 MHz and the minority density ratio $n_{^3He}/n_e$ is assumed to be 0.02. Fundamental and harmonic heating of electrons and various ion species are computed.

High values of the normalized pressure β_n have a risk of triggering Neoclassical Tearing Modes (NTM's) deleterious to confinement [4]. Control of NTM's in ITER is thought possible using ECRH, and so a system of ECRH launched from rapidly-steerable upper antenna is planned. NTM control is simulated by 4 MW of ECRH injected up to 700 s for this reason.

The ECRH system will have multiple roles: heating, current drive, and NTM suppression. Both the heating (ECH) and the current drive (ECCD) profiles are calculated. The ECRH is assumed to be launched from three equatorial launchers and two upper launchers. The frequency is assumed to be 170 GHz, launched in O-mode. The divergence of the rays is assumed to be narrow (1.2 deg). Locations and assumed angles are shown in Table II. Elevation and plan views of sample rays are shown in Figs. 3.

3. Plasmas Studied

The plasma regime studied is the H-mode which is considered to be the baseline for ITER [3]. The toroidal field is 5.3 T and the flattop plasma current I_p is 15 MA, with edge safety factor $q_{98} = 3.7$.

In current experiments the H-mode is generally seen when the heating power is above a threshold P_{LH}. Some experiments find that $P_{\rm ext}$ needs to be up to 50 per cent higher than P_{LH} for full H-mode energy confinement [5]. This complication is not modeled here. If the heating power drops below P_{HL}, a back transition occurs. There is considerable uncertainty of both P_{LH} and P_{HL} for ITER since the physics of the L-H transition and the pedestal are not well understood. Database values for P_{LH} have been used to extrapolate to ITER [6, 7]. Some experiments indicate that there is hysteresis in the transition, with P_{HL} being considerably lower than P_{LH} [8, 9].

One of the characteristics of the H-mode is a pedestal region near the edge, beyond which the density and temperature profiles decrease precipitously. The values of the temperatures at the top of the pedestal, $T_{\rm ped}$ are important boundary conditions for core temperature predictions. Differences in ion and electron temperatures at the pedestal are ignored here for simplicity. Databases for $T_{\rm ped}$ predict a wide range for ITER, e.g., 2.9 keV from the PEDESTAL module [10] in PTRANSP and 4.5 keV [11]. High values are beneficial for achieving high fusion yield, but have unwanted side-effects. Wide pedestal widths cause Edge Localized Modes (ELM's) with dangerous amounts of power deposition on the first wall [12]. Various ELM mitigation schemes are being studied. For this paper, three values of $T_{\rm ped}$ are assumed: 2.9 (from PEDESTAL), 4.1, and 5.2 keV. The scans are summarized in Table III.

The traditional assumption for the baseline electron density profile n_e is flat out to the top of the edge pedestal. The baseline assumption is that the flattop $n_e(0)$ is $1.0 \times 10^{20}/m^3$, so that the steady state Greenwald fraction ($\bar{n}_e/\bar{n}_{\rm GW}$ with $\bar{n}_e$ the line-average, and $\bar{n}_{\rm GW} \equiv I_p/(\pi a^2) \times 10^{20}/{\rm m}^3$) is 0.86, considered sufficiently low for good confinement.

There is uncertainty about whether n_e will actually be flat in ITER. Studies of the dependence, on plasma collisionality ν_*, of the density peaking (defined by $n_e(0)/ < n_e >$ where $n_e(0)$ is the central density and $< n_e >$ is the volume-average) indicate a peaking as ν_* reduces. The collisionality in ITER should be small compared to values measured in present high-performance H-mode plasmas since the electron temperature T_e is expected to be considerably higher than achieved.

Extensive database studies of peaking versus ν_* are available from JET [13, 14], ASDEX [15], TCV [16], and JT-60U [17]. There is evidence that ν_* is the dominant predictor of n_e peaking. Peaking of n_e and minimal peaking of the impurity densities would suggest increased performance since $P_{\rm DT} \propto n_D(0) n_T(0)$.

There are also theoretical arguments for an inward particle pinch [18–20]. These papers link the pinch to drift wave instabilities. The GLF23 and Weiland [21] models have been used to predict the n_e peaking versus ν_* in present experiments, with good agreement, and predict modest peaking in ITER.

The extrapolations to ITER are not conclusive since many of the anticipated plasma parameters will be very different in ITER. Examples are the mix of D and T, the central sink of D and T, the central source of ash, and the low rate of central fueling. Further physics-based extrapolations are needed for added credibility.

The density prediction capabilities of GLF23 and Weiland models have been incorporated into PTRANSP, and are being tested. Density treatment in PTRANSP is especially complicated due to the multiple modes of treating density (following the legacy of density analysis in TRANSP), and to the need for multiple ion species for realistic simulations of ITER (and present experiments).

As is standard for ITER modeling, the impurities are assumed to be beryllium with $n_{Be}/n_e = 0.02$, argon with $n_{Ar}/n_e = 0.0012$, ^{3}He minority (with $n_{min}/n_e = 0.02$), and the thermalized and recycled helium ash. The argon is assumed to be puffed in to increase radiation loss,

and thus to decrease the convected and conducted power flows, which need to be below a ceiling of about 110 MW. More argon may be needed for more radiation loss in plasmas having too high power flows. The anticipated trace amounts of other impurities such as carbon and tungsten are neglected, as is usual for ITER predictions.

The ash transport and recycling also can play important roles in the steady state fusion performance. Profiles of ^{4}He transport coefficients have been measured in TFTR DD and DT plasmas [22], and in JT-60U H-mode plasmas [23] with the results that the He velocity pinch profile is inward at most radii. It would be detrimental for ITER performance if a large inward pinch $V_{\rm ash}$ were found, unless a sufficiently large diffusivity $D_{\rm ash}$ were also found.

The physics of He (and other impurity) transport in tokamak plasmas is not well understood. Reference [20] has predicted ash profiles with benign peaking in the case of ITER H-mode plasmas with GLF23-predicted peaked n_e. Some nonlinear gyrokinetic simulations of turbulent-driven He transport in ITER-like plasmas indicate that the transport is complicated, with different wavenumbers transported at differing rates and even in different directions. The values of the assumed constant $D_{\rm ash}$ and $V_{\rm ash}$ for the physics scans are in Table III. In the cases where the pinch is inward ($V_{\rm ash}$ negative) the ash density becomes peaked on axis.

4. PTRANSP models

Most predictions of $P_{\rm DT}$ and $Q_{\rm DT}$ in ITER have assumed steady state profiles. The assumption of steady state prevents systematic investigation of consequences of reducing $P_{\rm ext}$. Also neglecting time-dependence misses important phenomena such as slow accumulation of the helium ash and the redistribution of species, energy, and magnetic field by sawteeth.

Here the PTRANSP code [1] is used for detailed time-dependent integrated modeling. PTRANSP is a new name for the TRANSP code, with P reflecting major upgrades in predictive capabilities. There is extensive and ongoing verification and testing of PTRANSP [1, 2].

The procedure is to first use the TSC code [24] to startup and to feedback control the plasmas consistent with the planned ITER coils and circuit equations. The ramp up, steady state, and ramp down are modeled. The electron density profile n_e is prescribed. The assumed profile is the standard baseline n_e (flat out to the top of the edge pedestal). The density is ramped linearly to steady state values after 160 s. The n_e profile is shown in Fig. 4. The total plasma current is ramped to the standard 15 MA at 100 s, as shown in Fig. 5.

The TSC time-evolving plasma boundary is input to PTRANSP for detailed computation of the heating, current drive, torque, fueling, and plasma equilibria. The runs were set up to yield good radial and time resolution.

It is necessary to predict T_i profiles to predict $P_{\rm DT}$. Also T_i and T_e profiles are needed to calculate heating. The GLF23 model [25, 26] and $T_{\rm ped}$ assumptions are used here since GLF23 predicts T_i and T_e profiles in approximate agreement with current H-mode plasmas [27]. The numerical algorithm for achieving solutions to the stiff GLF23 equations in PTRANSP has recently been improved [28]. Up to 30 Newton iterations are used here.

Predicting toroidal rotation is also important since toroidal rotation is needed to avoid locked modes, and since rotation contributes to flow shear which might reduce transport, increasing $P_{\rm DT}$. The flow shear is computed in GLF23 from the radial electric field E_r profile, which is calculated from radial force balance. The poloidal rotation contribution is computed in PTRANSP using NCLASS [29]. The pressure gradient contribution is calculated from the plasma profiles. For the heating mixes with NNBI, toroidal rotation is predicted to dominate the force balance in the core, so predicting the toroidal rotation contributions is important for assessing the need for NNBI.

GLF23 has been used to predict large rotation rates and enhanced $P_{\rm DT}$ in ITER [30]. The ability to predict toroidal rotation using GLF23 in PTRANSP has been improved recently [2], but these predictions are not as thoroughly tested in present experiments as are the temperature predictions. An alternative assumption is also studied: setting $\chi_\phi/\chi_i = 0.5$. This value is chosen since it is roughly midway in the range measured in present experiments. Results from both predictions are compared.

At the start of the $P_{\rm ext}$ the central electron density has ramped to $0.5{\times}10^{20}/m^3$, half of the flat-top density. One advantage of early $P_{\rm ext}$ is that database results for P_{LH} indicate an increase with density. However, a trade-off is needed in when to start the NNBI since high power NNBI cannot be started at too low density due to the danger of excessive shine-through power over-heating the far side of the vacuum vessel.

PTRANSP uses Monte Carlo methods [31, 32] to calculate beam deposition, beam torque, as well as the slowing down, pitch-angle scattering, and thermalization of beam ions and fusion ions. For the simulations presented here, the number of Monte Carlo particles used is 1000 for the beam ions and alpha particles. This number of samples gives fairly smooth beam heating profiles. Examples of heating profiles are shown in Fig. 6.

The TORIC code [33] is used to model the ICRH. The number of poloidal modes is 32. The number of toroidal mesh points is 64. The number of radial mesh points is 203. PTRANSP can run TORIC with a spectrum symmetric in the toroidal wave number n_ϕ. For the runs used here the spectrum is assumed to have two peaks at $\pm$ one value of $|n_\phi|$. The choice used here is $|n_\phi| = 27$, which is calculated to be the peak in the vacuum spectrum. For

the standard DT H-mode plasmas the corresponding parallel indices are calculated to be $n_{||}(0) = 3.84$, and the equivalent wave numbers $k_{||}$ are 4.23 m^{-1}.

The antenna position is indicated in Fig. 7, along with the plasma boundary and vacuum vessel. The position of the antenna cannot be too close to the vacuum vessel, which is assumed to be perfectly conducting in TORIC, because image currents would affect the computed wave patterns in the plasma.

An example of the resonance locations and heating fractions on ions and electrons for one case is shown in Table IV. The ^{3}He resonance is 20 cm past the magnetic axis. Table IV shows that most of the power is deposited on ^{3}He and electrons. The resolution of the ICRH simulations has been checked using standalone TORIC runs increasing the numbers of poloidal modes from 32 to 64, 128, 256, and 512. Contour plots of ICRH waves and power depositions show increasing resolution as the number of modes increases. At the highest number tried, 512, there is evidence of a failure of numerical convergence or Finite Larmour Radius effects starting to appear. Examples of contours from the standalone run with 256 poloidal modes are shown in Figs. 8 and 9. The contours indicate strong, single-pass absorption, and a small amount of ion-cyclotron mode conversion near the axis.

ICRH results for similar PTRANSP-TORIC ITER simulations used in Ref. [1] at one time-step has been benchmarked with AORSA-CQL3D [34] (L. Berry, private communication 2008).

The TORAY code [35–37] is used to model the ECH/ECCD. TORAY launched 20 rays from each antenna at each time step, and used 251 radial zones. Examples of profiles of the ECH power deposition to electrons are shown in Fig. 10. The localized depositions from the upper antenna 4-5 are peaked near the locations of the q = 1.5 and 2 f;ux surfaces, which might be needed for NTM suppression. ECRH results for one of the PTRANSP-TORAY ITER simulations has been benchmarked with the GENRAY code [38] (R. Harvey, private communication 2008).

Sawteeth are expected to have significant effects on plasma profiles in the core. A variety of sawtooth models are available in PTRANSP. For this paper a modification of Kadomtsev mixing [39] is used. A fixed sawtooth period of 10 s is assumed.

PTRANSP is run in a mode using models for the pedestal and for the L-H transition [2, 10]. From PEDESTAL P_{LH} is around 50 MW at full density, and P_{HL} is lower by 25%. PEDESTAL predicts a width for the pedestal which is near 5 cm for the cases studied here. The value of the normalized pressure β_{Pol} is 96 per cent of its maximum value. The model predicts the pressure, n_eT_e at the top of the pedestal when P_{LH} is exceeded. With the assumed profile for n_e, the prediction for $T_{\rm ped}$ is 2.9 keV (which is lower, and thus more pessimistic for $P_{\rm DT}$ than some other predictions and extrapolations). The radial boundary where $T_{\rm ped}$ is applied is near $r/a = 0.97$. Predictions are not sensitive to this choice. $T_{\rm ped}$ from this model is used for Scan-1, and is scaled up by 1.4 for Scan-3 and by 1.8 for the other scans.

For simplicity, the ash transport is computed assuming an explicit constant diffusivity $D_{\rm ash}$ and radial pinch $V_{\rm ash}$. Scans 1-3 assumed an outward pinch. For the others, an inward pinch is assumed. If the transport is inward (minus sign for $V_{\rm ash}$), the ash profile peaks in the core. If the magnitude of $V_{\rm ash}$ is too negative PTRANSP does not give a steady state solution if $P_{\rm DT}$ is high since $n_{\rm ash}$ becomes too large in the core for the assumed n_e. This is seen in the simulations for some of the scans. Presumably in reality either n_e or the transport would change as $n_{\rm ash}$ becomes very peaked. PTRANSP does not yet have a tested integrated density prediction capability needed to model n_e along with D, T, and multiple impurities consistently.

5. Predictions for cases near critical values

This Section discusses predictions for scans with assumed parameters close to critical values, near which qualitatively different behavior for $P_{\rm DT}$ are predicted for the different mixes of $P_{\rm ext}$. The next Section compares predictions for scans with assumed parameters which are not close to critical values.

With the assumptions of Scans 1, 4, and 5 none of the heating mixes provide sufficient heating to maintain $P_{\rm DT}$ after 400 s (when $P_{\rm ext}$ is reduced from $\simeq$40 MW) as shown in Table III. As $P_{\rm ext}$ decreases, the total heating power drops below the assumed P_{HL} threshold, forcing a decrease in $T_{\rm ped}$. With all the heating mixes except three in Scans 4 and 5, the total ash profiles come to steady state modulated by the assumed sawtooth mixing. In Scans 4 and 5 the ash profiles are very centrally-peaked. For Scan-5 the five heating mixes reach a steady state before 400 s. For Scan-4, the heating mixes with zero or one NNBI (IC/EC and 1NB/IC/EC) come to a steady state until 400 s, with $P_{\rm DT}$ is 220-320 MW. The other three mixes with two or three NNBI terminate before 400 s. Figure 11 shows the predicted $P_{\rm DT}$.

The cause of early termination of the three mixes with two or three NNBI is that they have broader heating profiles, and slightly lower GLF23-predicted ion energy transport coefficients χ_i near the mid-radius. Thus they have higher T_i and $P_{\rm DT}$, but fail sooner as the central ash density becomes too high for the assumed $n_e(0)$, The ash profiles are not sufficiently broad to self-regulate by reducing the DT reaction and thus the ash source from thermalizing alpha ions. The two mixes with zero or one NNBI do self-regulate. For Scan-5 all the heating mixes self-regulate.

Scans 4-9 explore consequences of increasing $D_{\rm ash}$ while holding the other assumptions fixed. Predictions of

the ash profiles and evolutions of the central and volume-averaged ash densities for the heating mix 3NB/IC are shown in Fig. 12. For relatively small $D_{\rm ash}$ (scans 4 and 5) the predicted $P_{\rm DT}$ depends sensitively on $P_{\rm ext}$ and the heating mix. For values higher than these critical $D_{\rm ash}$ the predictions are less sensitive.

The effective charge profile $Z_{eff} \equiv \Sigma_j n_j Z_j^2/n_e$ indicates effects of impurity ion dilution on the DT fuel profile. The contributions of each ion with density n_j and charge Z_j is $n_j Z_j^2/n_e$. For a pure DT plasma $Z_{eff} = 1.0$. Profiles of the contributions to Z_{eff} for two of the cases are shown in Fig. 13. Figure Fig. 13-a) shows the 3NB/IC Scan-4 case that tops Fig. 11. Figure Fig. 13-b) shows 2NB/IC/EC Scan-2, which is not close to a critical combination of $D_{\rm ash}$ and $V_{\rm ash}$. In both cases the contributions from the ^{3}He minority, fast alpha, and beam ions are relatively small.

The recycling of helium from outside the main plasma plays an important role if the ash transport has an inward pinch [1]. The recycling coefficient R (defined as Γ_{in}/Γ_{out}, the ratio of the radial flows into and out from the plasma through the separatrix) is held constant at 0.7 here. If R were higher, $P_{\rm DT}$ would be lower (and zero at R = 1.0).

All the scans and heating mixes that achieved high steady state $P_{\rm DT}$ also obtained ignition when $P_{\rm ext}$ is reduced to zero. The ranges of $P_{\rm DT}$ are shown in the last column of Table III. This shows that none of the heating mixes with the assumptions of Scan-1, 4, and 5 can ignite. For Scan-3, three are predicted to ignite. Examples of the time dependencies of $Q_{\rm DT}$ for several scans are shown in Fig. 14.

6. Predictions for cases away from critical values

The various heating mixes are predicted to have different power depositions on the thermal ions and electrons, but the ion-electron equilibration rate is predicted to become rapid as the density increases to the steady state value. Examples of the early evolution of the central T_i and T_e for the various heating mixes (in the case of Scan-2) are shown in Fig. 15. Large core temparatures are seen transiently, with magnitudes correlated with the amount of NNBI power. Especially high $T_i(0)$ are predicted with the heating mix 3NB/IC. The predictions of lower core temperatures if the flow shear suppression is turned off are also shown for comparison. There are additional uncertainties in the predictions of the PEDESTAL model early as the density is ramping up since that model is based on measurements during approximately steady state plasmas.

Soon after the start of the NNBI the energy distribution of the beam ions is calculated to be strongly non-monotonic, peaked near the injection energy (1 MeV). Shortly thereafter the calculated distribution approaches a slowing-down distribution, but the distribution in pitch angle $v_{||}/|v|$ remains peaked near $v_{||}/|v| \simeq$ unity. High core temperatures, β_{beam}, and β_α lasting about 50 s are predicted. Examples are shown in Fig. 15-c. These high values, and the asymmetries in the beam distribution are predicted to drive strong Toroidal Alfvén Instabilities. The temperature, β, and pitch angle asymmetry drives of these instabilities have been studied [40, 41].

At steady state the predicted T_i and T_e profiles converge to similar values for all assumed heating mixes in the physics assumption scans with $\chi_\phi/\chi_i = 0.5$. Results are shown in Figs. 16. For Scan-11 using GLF23 to predict v_{tor}, the predicted v_{tor} is six times larger, and a wider range of T_i is predicted, due to the flow shear suppression of transport caused by the NNBI-driven v_{tor}. An example is shown in Figs. 17. The predicted range of values for $P_{\rm DT}$ and $Q_{\rm DT}$ are similar for the alternative assumptions for predicting v_{tor}.

The highest value predicted for $P_{\rm DT}$ is 703 MW for Scan-11 (GLF23-predicted rotation) with the heating mix 3NB/IC. This is maintained from 140 to 400 s, after which $P_{\rm DT}$ decreased to 522 MW. Since $P_{\rm ext}$ is stepped down from 43 to 34 MW at 300 s, then to 4 MW (simulating NTM control) at 400 s, then to zero, $Q_{\rm DT}$ increased from 17 to 22 after 300 s, and increased to effectively infinity after 400 s. The ranges of $P_{\rm DT}$ are listed in the last two columns of Table III.

Since the GLF23 rotation predictions are not as well tested as the temperature predictions, the predictions from Scan-11 should be considered more tentative. For the other scans with the more conservative assumption of $\chi_\phi/\chi_i = 0.5$, the next highest values of $P_{\rm DT}$ are from Scans 8 and 9 which both achieved 597 MW between 200 and 300 s. The next is Scan-2 with 589 MW. For these three scans, the 2NB/EC heating mix gave the maximum. The spread of $P_{\rm DT}$ over heating mixes is 15%.

7. Discussion

One uncertainty is how the H-mode and pedestal will respond to the shift from external to alpha dominated heating. The ion and electron heating power profiles will change. Examples of the total, ion, and electron heating for one of the Scan-2 mixes is shown in Fig. 18-a). Experiments have not identified obvious direct changes in the pedestal when the heating changes, but there can be indirect effects via changes in beta or collisionality.

Examples of the computed values of the global normalized pressure, $\beta_n \equiv < \beta_{tor} > aB/I$ are shown in Fig. 18-b). The volume-average of $\beta_{tor} \equiv 2\mu_0 P/B^2$ is used, where P is the total pressure normalized by the Troyon factor with plasma current [MA], minor radius [m], and vacuum toroidal magnetic field [T]. They range between 1.35-1.55 for Scan-1, and from 1.6 to 2.2 for the other scans. The standard assumption for the baseline

ITER H-mode ("Scenario2") is 1.8. In cases with ignition, there is a slight decrease in β_n as the heating power changes as $P_{\rm ext}$ decreases.

Experiments in DIII-D [42] indicate that $\beta_{n,ped}$ ($\equiv$ the local β_n at the top of the pedestal) decreases as the global β_n decreases. Calculations of peeling-ballooning stability of the edge barrier [43] find that $\beta_{n,ped}$ is a useful figure of merit for describing the pedestal stability limit. The recently developed EPED1 pedestal model [44] combines peeling-ballooning stability calculations with a second constraint based on local kinetic ballooning mode onset to allow prediction of the pedestal height and width.

EPED1 model calculations for some of the PTRANSP ITER baseline cases predict a pedestal height of $\beta_{n,ped} \simeq$ 0.6-0.7 [44], approximately consistent with the results shown in Fig. 18-c). The EPED1 model does have a dependence on global beta because the Shafranov shift affects peeling-ballooning stability. However, for ITER, in the range of β_n values discussed here, the variation in the EPED1 predicted pedestal height with global beta is fairly small [P.B. Snyder, private communication 2009].

The computed radiative power losses range up to 29 MW from bremsstrahlung, 7 MW from line radiation, and 7 MW from net synchrotron radiation. The net charge-exchange loss from interaction with recycling neutrals is calculated to be localized near the edge and small ($\simeq$ 1 MW), but could be higher if the wall recycling rate is large.

The values of $\tau_{\rm E}$ defined by the ratio of the total thermal energy and the conductive, convective, radiation, and net charge exchange losses, are in the ranges 2.2-2.3 s for Scan-1, and 3.3-5.3 s for the other scans. These values are not decisive indicators of ignition. The values for the triple-product, $n_e T_i \tau_{\rm E}$ (with n_e and T_i volume-averaged to r/s=0.2) are in the range 65-80 [10^{20}-keV-s/m^3] for ignition. The ratio of ash to electrons varied from 1.5 % for Scan-1 and 10 % for Scan-4. The values of the ash particle confinement, $\tau_{\rm ash}$ range from 3-110 s. The ratio $\tau^*_{\rm ash}/\tau_{\rm E}$ is decisive for ignition. The simulations with ignition have this ratio in the range 3-80.

Global zero-dimensional studies of DT ignition in the presence of radiative energy loss and helium ash confinement have found [45] closed contours for the triple-product, $n_e T_i \tau_{\rm E}$ versus T_i, parameterized by the ratio $\tau^*_{\rm ash}/\tau_{\rm E}$. The accessible ignition region is found to vanish as this ratio increased above 15. The conditions found in [45] for the triple-product and T_i with large $\tau^*_{\rm ash}/\tau_{\rm E}$ are around 90 [10^{20}-keV-s/m^3] and 17 [keV]. The higher values found here for $\tau^*_{\rm ash}/\tau_{\rm E}$ are in Scans with inward ash pinches, and are considerably higher than the maximum found in a 0D analysis.

Large extrapolations are needed to extrapolate many of the plasma parameters from present experiments to ITER. One such parameter is P_{LH}. To explore what could be expected if P_{LH} turns out to be much higher than expected, a set of heating mix predictions is done with P_{LH} scaled up a factor of three (to 150 MW at flattop) from the PEDESTAL values. Also $T_{\rm ped}$ is scaled down a factor of 0.8. The predicted evolutions of the heat flow into the region where the pedestal could form is compared with that required by the scaled up P_{LH} in Fig. 19-a). The plasma obtains the H-mode only between 110 and 120s. Plasma temperature profiles are shown in Fig. 19-b).

Examples of the neutron emission and $P_{\rm DT}$ from the five heating mixes are shown in Fig. 20. The plasmas obtain $Q_{\rm DT}$ around 2-4. The predicted values for β_n in the steady state L-mode phase range from 0.8 to 1.3.

8. Summary

The PTRANSP code with GLF23 is used to predict $P_{\rm DT}$ in the baseline ITER "scenario 2" H-mode with five assumed mixes of external heating and a variety of physics assumptions. Figure 1 and Table I show the heating mixes chosen, and Table III summarizes the physics assumptions and gives ranges of $P_{\rm DT}$ in phases with reduced $P_{\rm ext}$.

The predictions of temperature profiles and $P_{\rm DT}$ for the different heating mixes can differ significantly if conditions are close to marginal or critical values such as $P_{\rm ext}$ being close to threshold or $T_{\rm ped}$ being low or $D_{\rm ash}$ small if $V_{\rm ash}$ is inward. For instance, Table III shows that $P_{\rm DT}$ is sensitive to the heating mix near critical values of $D_{\rm ash}$. Examples of predictions of $P_{\rm DT}$ for Scan-4 are shown in Fig. 11.

The predictions of steady state temperature profiles and $P_{\rm DT}$ are comparable for all the heating mixes if conditions are not not close to marginal or critical values Examples of profiles with the toroidal rotation predicted assuming $\chi_\phi/\chi_i = 0.5$ are shown in Fig. 16. Ten % variation in the predicted $P_{\rm DT}$ are found. The anticipated toroidal rotation from the NNBI is estimated to increase $P_{\rm DT}$ about 10% Figure 14 shows examples of predictions with infinite $Q_{\rm DT}$ occurring after 400s.

GLF23 predicts much larger v_{tor} resulting from the NNBI torques. Combined with NCLASS predictions of v_{pol}, the flow shearing rates are predicted to significantly increase the T_i profiles. Examples are shown in Fig. 17.

Predictions of L-mode $P_{\rm DT}$ and $Q_{\rm DT}$ are obtained assuming P_{LH} turns out to be larger than expected. Results are shown in Figs. 19 and 20.

The heating mixes with more NNBI are predicted to have the advantage over ones with less by having increased v_{tor}, $P_{\rm DT}$ and $Q_{\rm DT}$. In case the ITER capabilities turn out to be close to critical or marginal parameters, these increases could be crucial for success. On the other hand, they have potential disadvantages if maximum power is needed when the density is low, such as causing more shine-through power to the inner armor. Also NNBI (and ICRH) have the potential disadvantage

of causing Alfvén wave-induced fast ion losses especially during the low density ramp up and ramp down phases.

There are many consequential physics processes that cannot yet be modeled in PTRANSP. These include ELMs, MHD, disruptions, and fast ion wave and MHD interactions.

An important caveat about this study is that the plasmas predicted have the standard flat electron density profile. Results could be quite different with more peaked profiles.

Another caveat is that in plasma regimes other than the standard H-mode, the heating or current drive could play important roles in triggering self-organized states. For instance, in the Hybrid, Advanced Inductive, and Steady State scenarios the total plasma current could be lower and thus the externally driven and bootstrap currents could be relatively larger.

There are many uncertainties about the technology and physics challenges that ITER will face, so it is not possible to make definitive predictions about ITER performance. Having flexibility of choosing among a variety of heating schemes could prove to be important when ITER is faced with unforeseen challenges.

Acknowledgements

The author wishes to thank the PTRANSP development teams at PPPL, Lehigh, GA, and LNL. This research was supported by the U.S. Department of Energy under contract number DE-AC02-09CH11466

* Electronic address: budny@princeton.edu

[1] Budny R.V., Andre R., Bateman G., Halpern F., Kessel C., Kritz A., and McCune D., Nucl. Fusion **48**, (2008) 075005.
[2] Halpern F.D., Kritz A.H., Bateman . G., *et al.*, Phys. Plasmas **15** (2008) 062505.
[3] Campbell D.J., Plasma Phys. **8** (2001) 2041.
[4] Lahaye R., Osborne T.H., Rettig C.L., *et al.*, Nucl. Fusion **35** (1995) 988.
[5] Sartori R., Saibene G., Horton L.D., Becoulet M., *et al.*, Plasma Phys. Control. Fusion **46** (2004) 723.
[6] Ryter F., the H-mode Threshold Database Group, Plasma Phys. Controlled Fusion **44** (2002) A415.
[7] Martin, Y.R. and ITPA CMDB H-mode Threshold Database Working Group, J. of Physics Conference Series **123** (2008) 012033.
[8] Kallenbach A., Dux R., Bosch H.-S., *et al.*, Plasma Phys. Controlled Fusion **38** (1996) 2097.
[9] Mertens S V., Kaufmann M., Neuhauser J., *et al.*, Nucl. Fusion **37** (1997) 1607.
[10] Onjun T., Bateman G., Kritz A.H., and Hammett G., Plasma Phys. Controlled Fusion **45** (2003) 1939.
[11] Sugihara M., Mukhovatov V., Polevoi A., and Shimada M., Plasma Phys. Controlled Fusion **45** (2003) L55.
[12] Hawryluk R.J., Campbell D.J., Janeschitz G., Thomas P.R., *et al.*, Nucl. Fusion **49** (2009) 065012.
[13] Weisen H., Zabolotsky A., Angioni, Furno C.I., *et al.*, Nucl. Fusion **45** (2005), L1.
[14] Weisen H., Zabolotsky A.,Maslov M., Beurskens M., Giroud C., *et al.*, Plasma Phys. Control. Fusion **48** (2006) A457.zev:200
[15] Pereverzev G.V., Angioni C., Peeters A.G., and Zolotukhin O.V., Nucl. Fusion **45** (2005), 221.
[16] Zabolotsky A., Weisen H., and TCV Team, Plasma Phys. Control. Fusion **48** (2006) 369.
[17] Takenaga H., Tanaka K., Muraoka K., Urano H., Oyama N., *et al.*, Nucl. Fusion **48** (2008) 075004.
[18] Angioni C., Peeters A.G., and Pereverzev G.V., *et al.*, Nucl. Phys. Rev. Letters **90** (2003), 205003.
[19] Angioni C., Weisen H., and Kardaun O.J.W.F, and Maslov M., *et al.*, Nucl. Fusion **47** (2007), 1326.
[20] Angioni C., Pereverzev G.V., Bottino A., Candy J., Dux R., Fable E., Hein T., and Waltz R.E., Nucl. Fusion **49** (2009), 055013.
[21] J. Weiland and A. Jarmén and H. Nordman, Nucl. Fusion **29** (1989), 1810.
[22] Synakowshi E.J., Bell R.E., Budny R.V., *et al.*, Phys. Rev. Lett. **75** (1995) 3689.
[23] Takenaga H., Nagashima K., Sakasai A., *et al.*, Nucl. Fusion **39** (1999) 1917.
[24] Kessel C.E., Giruzzi G., Sips A.C.C., *et al.*, Nucl. Fusion **47** (2007) 1274.
[25] Waltz R.E., Staebler G.M., Dorland W., *et al.*, Phys. Plasmas **4** (1997) 2482.
[26] Kinsey J.E., Staebler G.M., and Waltz R.E., Fusion Science and Technol. **44** (2003) 763.
[27] Kinsey J.E., Staebler G.M., and Waltz R E., Phys. Plasmas **15** (2008) 055908.
[28] Jardin S.C., Bateman G., Hammett G.W., and Ku L.P., J. Comp. Phys. **227** (2008) 8769.
[29] Houlberg W.A., Shang K.C., Hirshman S.P., and Zarnstorff M.C., Phys. Plasmas **4** (1997) 3230.
[30] Stabler, G.M. and JOHN, H. E. S., Nucl. Fusion **46** (2006) L6.
[31] Goldston R.J., McCune D.C., Towner H.H., *et al.*, J. Comput. Phys. **164** (2004) 421.
[32] Pankin A., Bateman G., Budny R., *et al.*, Comput. Phys. Commun. **43** (1981) 61.
[33] Brambilla M., Plasma Phys. Controlled Fusion **44** (2002) 2423.
[34] Jaeger E.F., Berry L.A., Azevedo E.F., Barnett R.F., *et al.*, Phys. Plasmas **15** (2008) 072513.
[35] Batchelor D.B., Goldfinger R.C., Nucl. Fusion **20** (1980) 403.
[36] Kritz A.H., Hsuan H., Goldfinger R.C., and Batchelor D.B., 1982 Conf. Proc. 3rd Int. Symp. on Heating in Toroidal Plasmas ECE (Brussels, Belgium) **2** (1982) 707.
[37] Prater R., Farina D., Gribov Y., *et al.*, Nucl. Fusion **48** (2008) 035006.
[38] Smirnov A.P. and Harvey R.W., Bull. Amer. Phys. Soc., 40, 1837, Abstract 8P35 (1995).
[39] Kadomtsev B.B., Sov. J. Plasma Phys. **1** (1975) 389.
[40] Gorelenkov N.N., Berk H.L., Budny R.V., *et al.*, Nucl. Fusion **43** (2003) 594.
[41] Gorelenkov N.N., Berk H.L., Budny R.V., Nucl. Fusion **45** (2005) 226.
[42] Leonard A.W., Groebner R.J., Osborne T.H., *et al.*, Phys. of Plasmas **15** (2008) 056114.
[43] Snyder P.B., Wilson H.R., Osborne T.H., and Leonard A.W., Plasma Phys. Controlled. Fusion **46** (2004) A131.
[44] Snyder P.B., Groebner R.J., Leonard A.W., Osborne T.H., and Wilson H. R., Phys. Plasmas **16** (2009) 056117.
[45] Rebhan E., Vieth U., Reiter D., and Wolf G.H., Nucl. Fusion **36** (1996) 264.

Heating type	NNBI [MW]	ICRH [MW]	ECRH [MW]
2NB/EC	34-17	0	40-30-20
2NB/IC/EC	34-17	20-10-0	20
IC/EC	0	20-10-0	53-47
3NB/IC	50-33	20-10-0	0
1NB/IC/EC	17-0	20-10-0	37

TABLE I: *External heating mixes considered. The total $P_{\rm ext}$ is approximately 73 MW from 80 to 130 s, then decreases to 40-50 MW until 300 s, then to 36-40 MW until 400 s, then to 4 MW of ECRH until 700 s. The time dependences are shown in Fig. 1.*

Launcher	Ant 1	Ant 2	Ant 3	Ant 4	Ant 5
Major Radius [m]	8.50	8.50	8.50	6.48	6.45
Height [m]	0.01	0.61	1.21	4.11	4.20
Poloidal angle [deg]	90.0	90.0	90.0	146.0	150.0
Toroidal angle [deg]	210.0	215.0	218.0	200.0	202.0

TABLE II: *ECH launcher geometry. Antennae 1-3 are the equatorial launchers and antennae 4-5 are the steerable upper launchers for NTM control. The toroidal angles advance counter-clockwise viewed from above starting at the antenna.*

Assumptions Units	$T_{\rm ped}$ [keV]	χ_ϕ	$D_{\rm ash}$ $[m^2/s]$	$V_{\rm ash}$ $[m/s]$	$V_{\rm ash}/D_{\rm ash}$ $[m^-1]$	$P_{\rm DT}$ (350s) [MW]	$P_{\rm DT}$ (750s) [MW]
Scan-1	2.9	$0.5\chi_i$	0.1	+0.1	+1.0	195-306	0
Scan-2	5.2	$0.5\chi_i$	0.1	+0.1	+1.0	486-589	486-530
Scan-3	4.1	$0.5\chi_i$	0.1	+0.1	+1.0	233-417	0-322
Scan-4	5.2	$0.5\chi_i$	0.1	-0.1	-1.0	0-208	0
Scan-5	5.2	$0.5\chi_i$	0.12	-0.1	-0.83	264-319	0
Scan-6	5.2	$0.5\chi_i$	0.15	-0.1	-0.67	347-389	311-339
Scan-7	5.2	$0.5\chi_i$	0.25	-0.1	-0.25	458-514	425-464
Scan-8	5.2	$0.5\chi_i$	0.50	-0.1	-0.20	522-597	497-508
Scan-9	5.2	$0.5\chi_i$	1.0	-0.1	-0.10	556-597	542-567
Scan-10	5.2	$0.5\chi_i$	1.0	-1.0	-1.0	472-533	458-500
Scan-11	5.2	GLF23	1.0	-1.0	-1.0	528-703	532-556

TABLE III: *Scans in $T_{\rm ped}$, momentum prediction, and ash transport. The ash recycling coefficient at the plasma boundary [1] is kept fixed at 0.7). The last column gives the ranges in $P_{\rm DT}$ for the five heating mixes after $P_{\rm ext}$ is turned off.*

ion species	Fundamental	Harmonic
Thermal T	(-3.1) 0.0	(0.2) 12.4
Thermal D	(-1.5) 0.8	(3.4) 0.0
Ash	(-1.5) 0.1	(3.4) 0.0
Be impurity	(-1.5) 0.3	(3.4) 0.0
B impurity	(-1.5) 0.1	(3.4) 0.0
Fast ^{3}He (minority)	(+0.2) 49.7	(6.7) 0.0
Fast α (DT)	(-1.5) 0.1	(3.4) 0.0
Fast D (beam)	(-1.5) 0.0	(3.4) 0.0
electrons	from FW	from IBW
	36.5	0.2
Fast ^{3}He heating	ions	electrons
	78	23

TABLE IV: *Resonance locations ([m] relative to the magnetic axis and partition fractions (%) of ICRH heating corresponding to the case of Scan-2 with heating mix 2NB/IC/EC at 250 s, with contours shown in Figs. 8-9. The magnetic axis is at R_0=6.39 [m]. The inner most radius is 4.19 [m] so the fundamental T resonance is not in the plasma. Likewise the outer most radius is 8.28 [m] so all but the T harmonic resonance are not in the plasma. The electron heating fractions from Fast Wave and Ion Bernstein Wave, and the fractions of heating of the thermal plasma by the slowing down ^{3}He are also given. Profiles of the total ion and electron power depositions are shown in Fig. 6-a).*

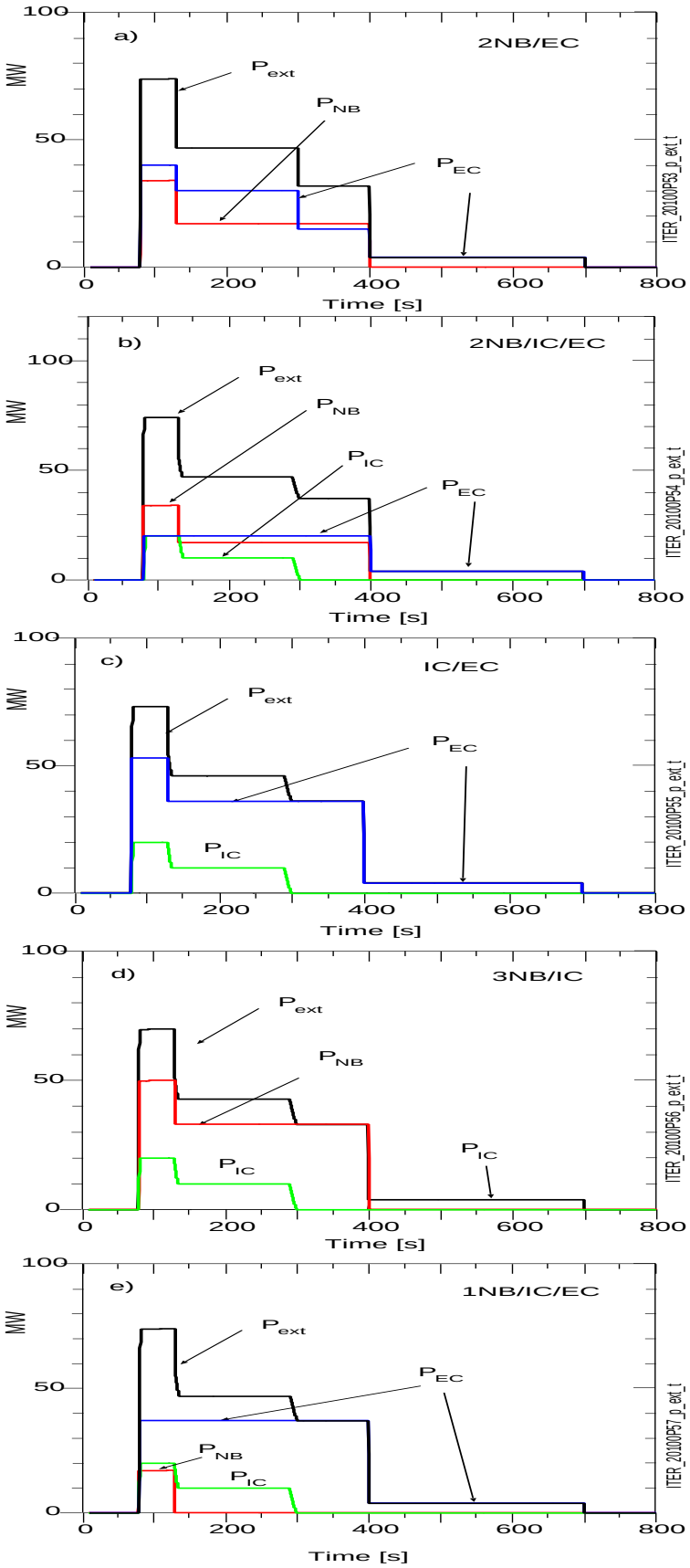

FIG. 1: Time traces of the various heating powers assumed, as summarized in Table I. The total $P_{\rm ext}$ was kept approximately fixed for comparisons.

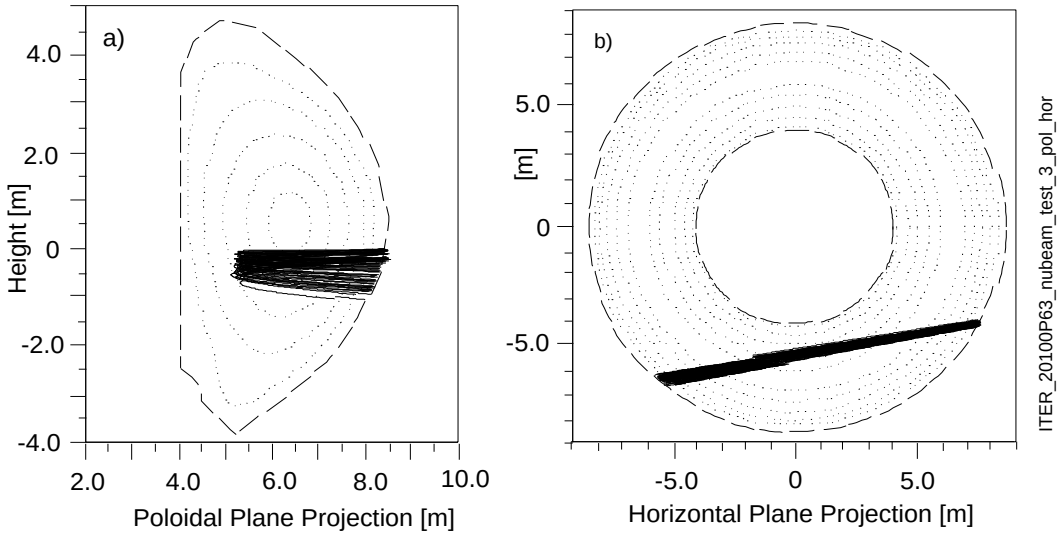

FIG. 2: Trajectories of D^0 from NNBI. The directions of the plasma current and toroidal field are assumed to be clockwise viewed from above. Thus the NNBI direction is the same as that of the plasma current.

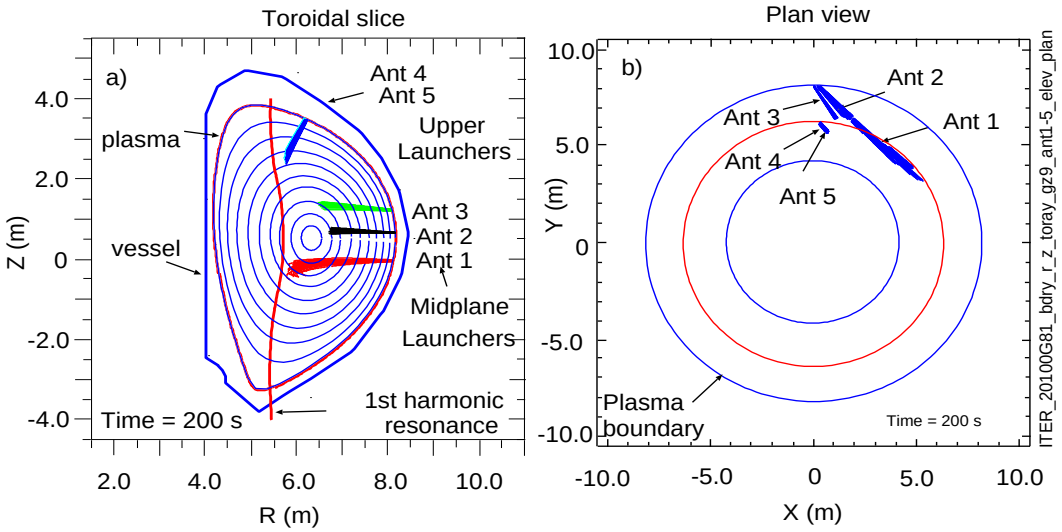

FIG. 3: ECCD rays from TORAY. The launching angles for the case shown differ slightly from the angles used in this paper and given in Table II.

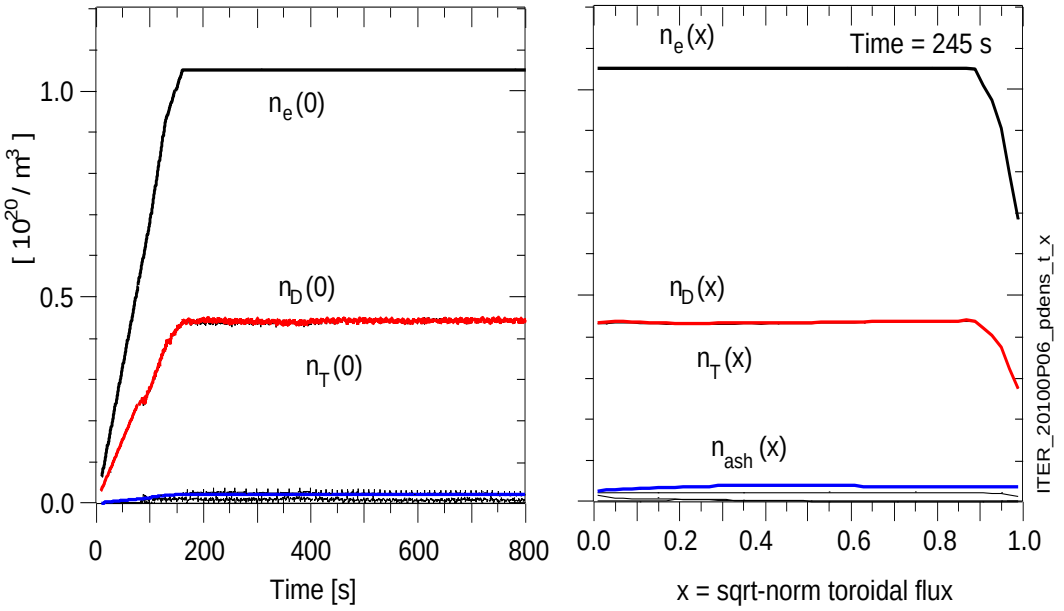

FIG. 4: Assumed electron density profile and calculated profiles of deuterium, tritium, and alpha ash for one of the heating mixes (2NB/EC) and physics scans (Scan-2).

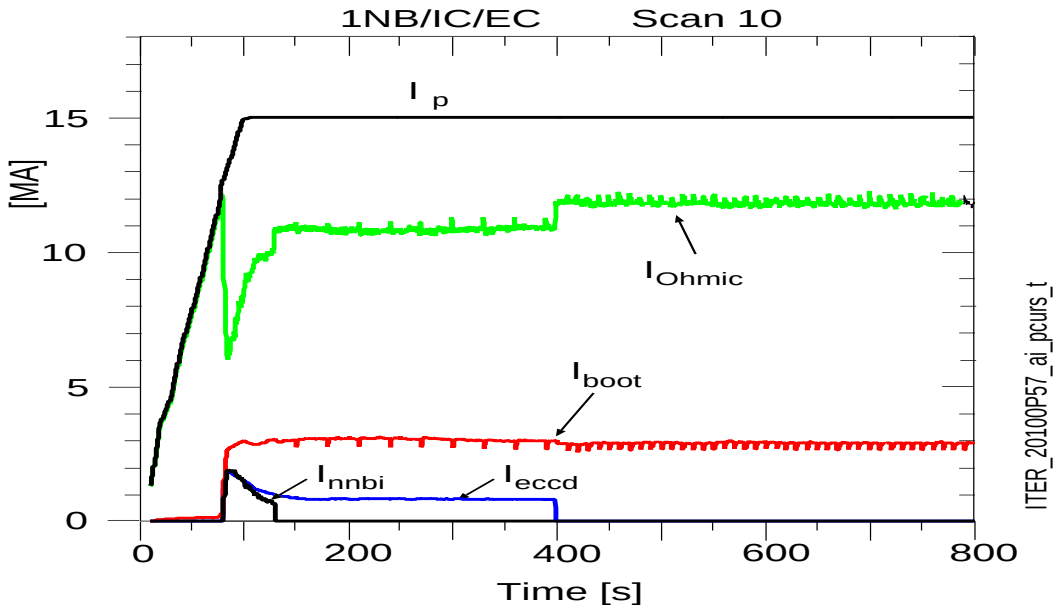

FIG. 5: Assumed total plasma current and calculated Ohmic, bootstrap, ECCD, and NNBI currents calculated for one of the heating mixes (1NB/IC/EC) and physics scans (Scan-10).

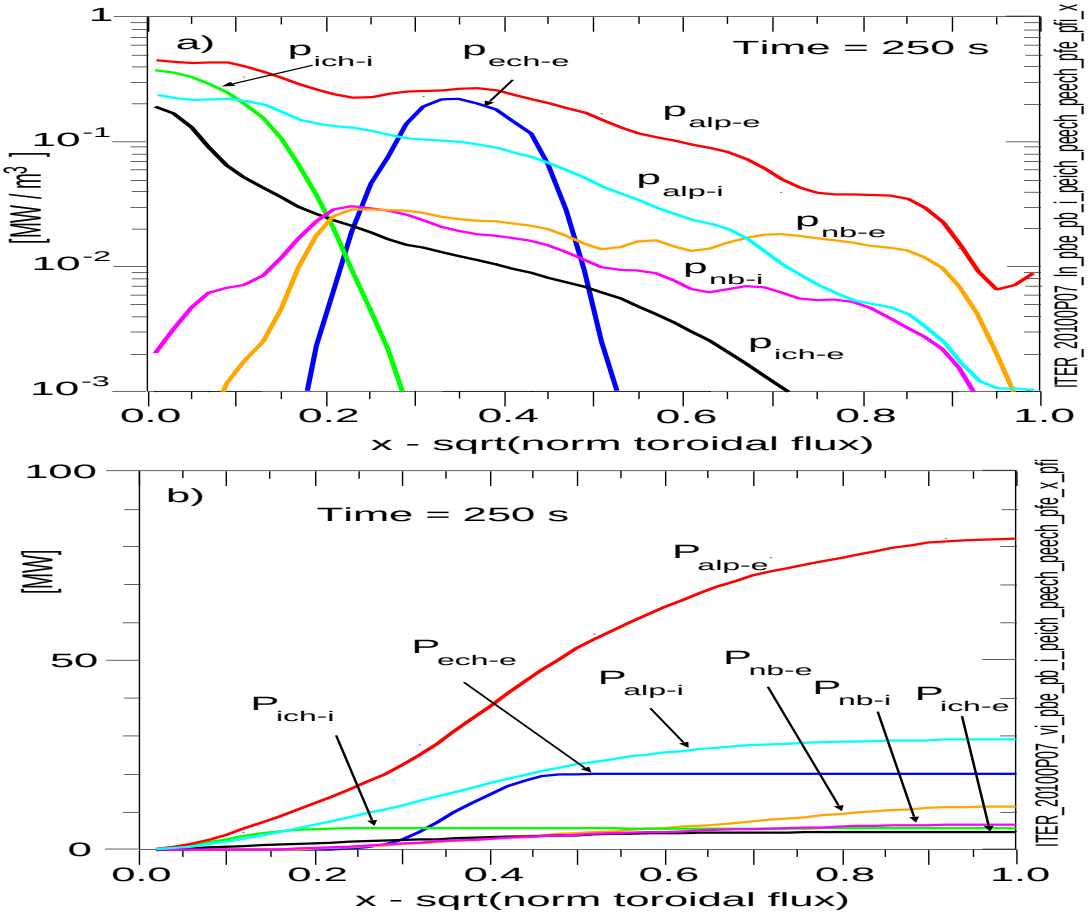

FIG. 6: a) profiles, and b) volume-integrated profiles of heating powers versus the square-root of the normalized toroidal flux. The example is for one of the heating mixes (2NB/IC/EC) and physics scans (Scan-2). The absorbed heating from the NNBI, ICRH, and ECRH are 17, 10, and 20 MW at the time shown.

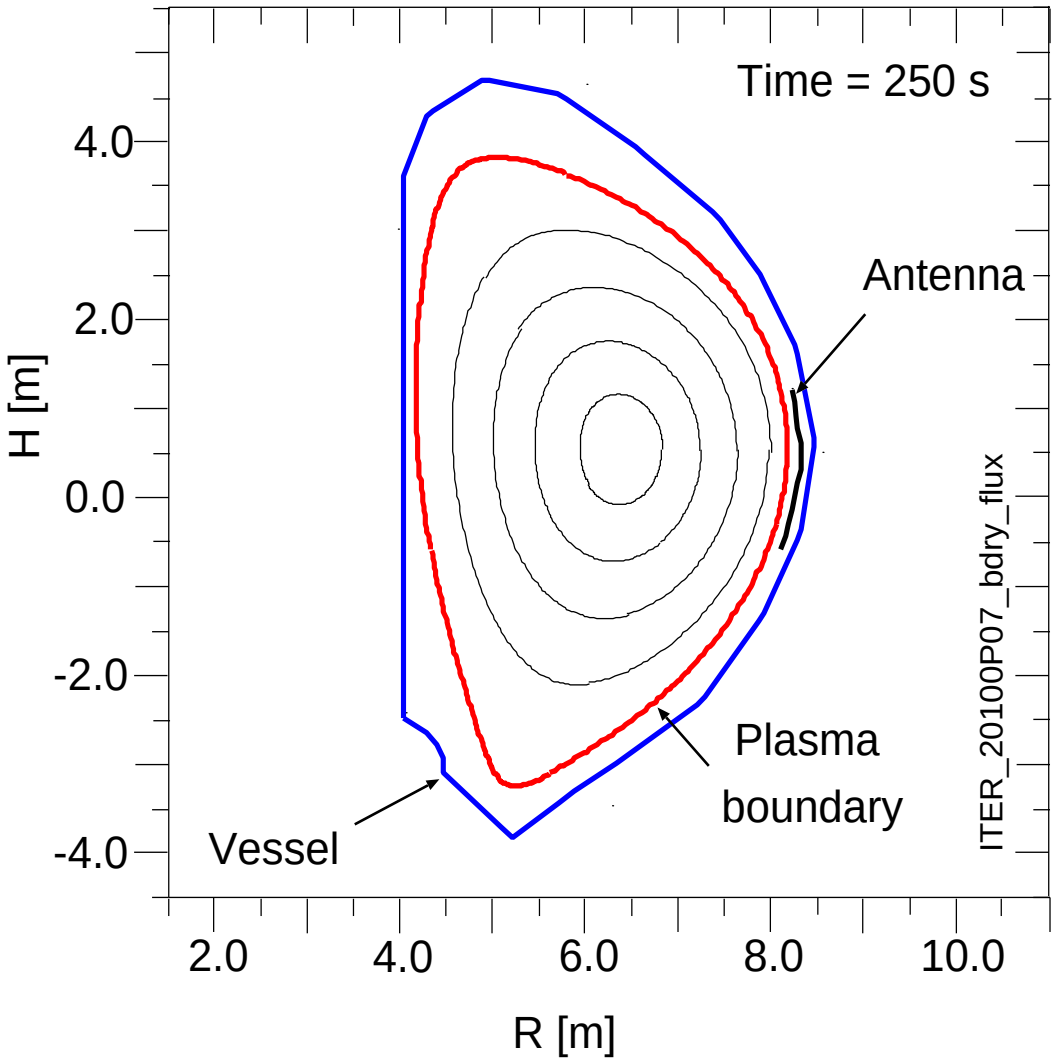

FIG. 7: Wall and antenna locations. The separation between the separatrix and antenna is 15-17 cm.

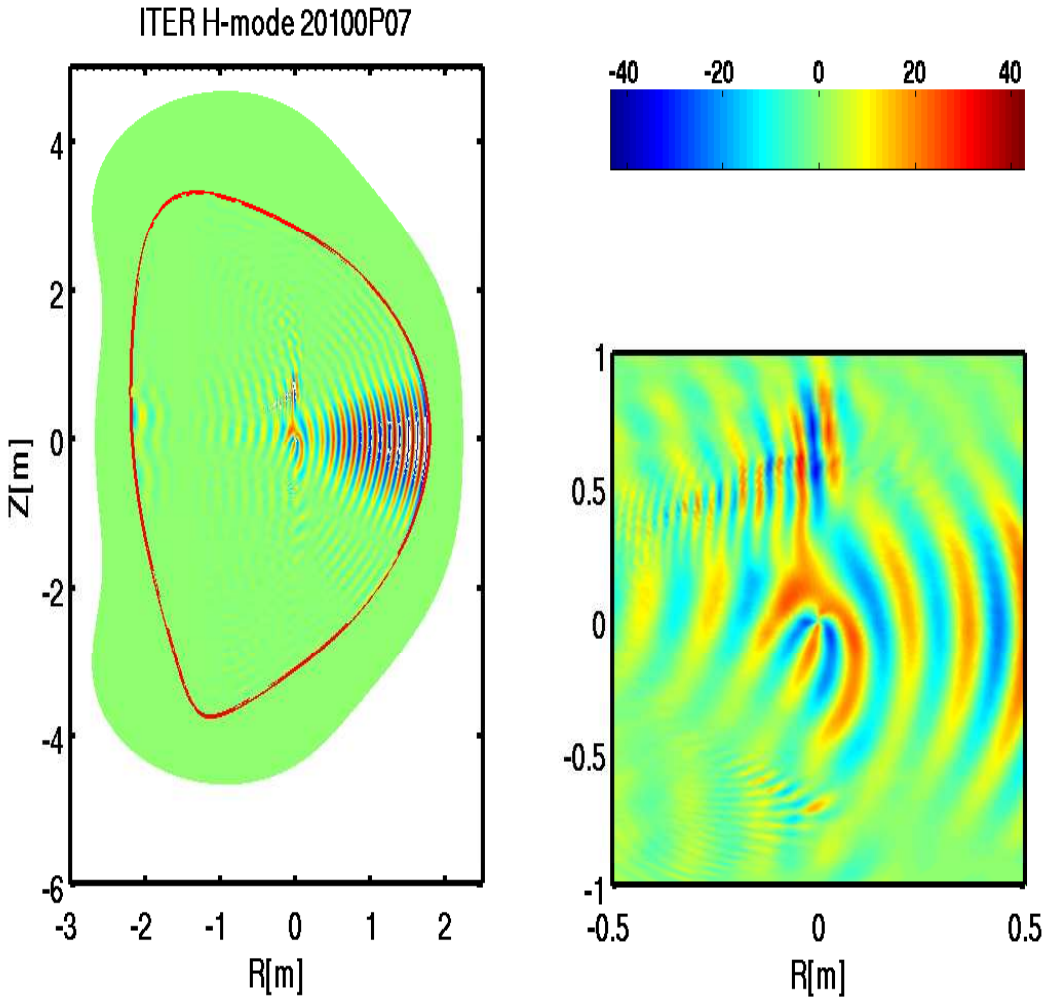

FIG. 8: Contours for the real part of E_+^2 from a simulation for Scan-2 with heating mix 2NB/IC/EC at 250 s. The color scale units are V/m per MW ICRH power absorbed. TORIC was run in standalone mode starting with inputs from PTRANSP using 32 poloidal modes, and increasing the number of poloidal modes to 256.

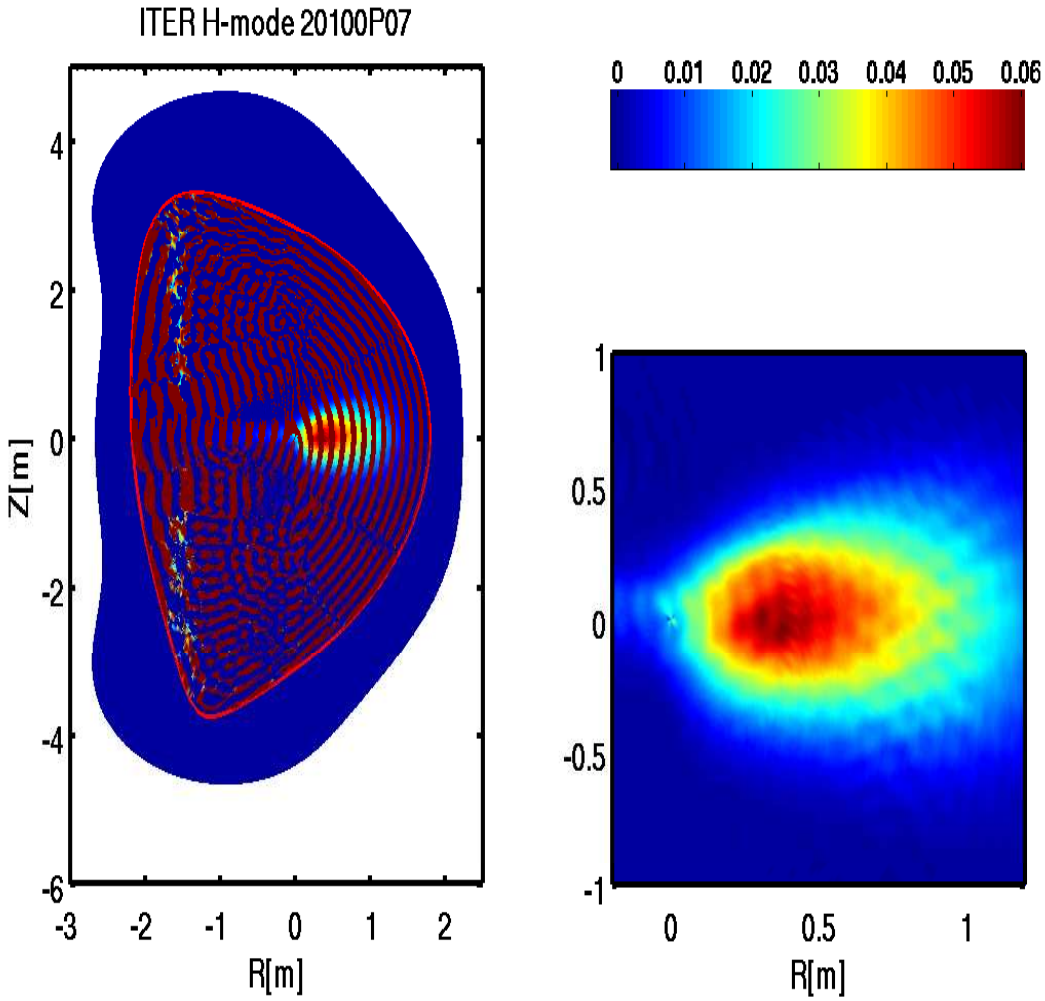

FIG. 9: Contours of ICRH power deposition directly to electrons. The color scale units are MW/m^3 per MW ICRH power absorbed. TORIC was run in standalone mode starting with inputs from PTRANSP using 32 poloidal modes, and increasing the number of poloidal modes to 256.

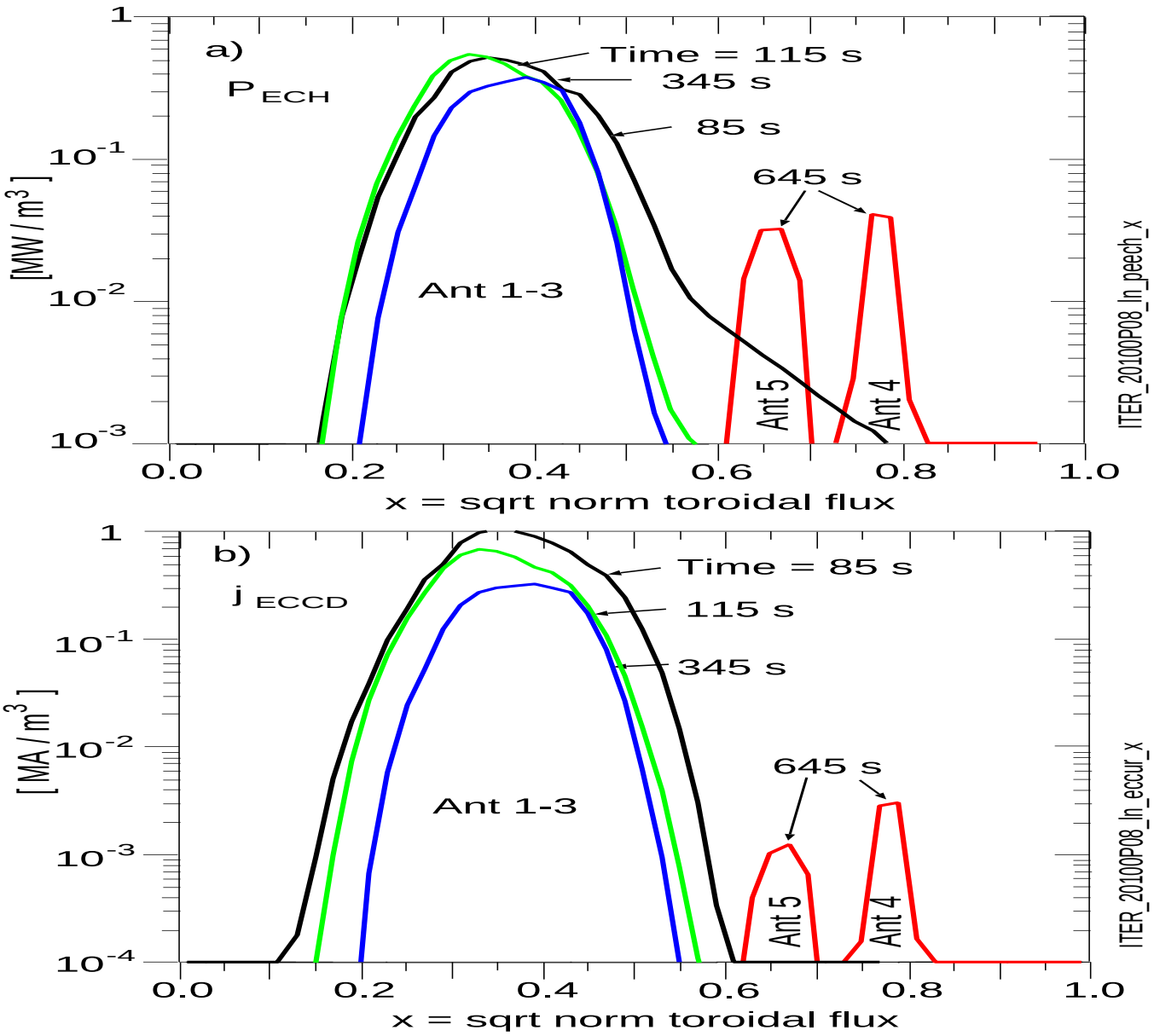

FIG. 10: ECH and ECCD profiles at four times for one of the heating mixes (IC/EC) and physics scans (Scan-2). The ECRH heating power (shown in Fig. 1-c) is 53 MW from 80 to 130 s, then drops to 36 MW until 400 s, (from the equatorial launchers), and then drops to 4 MW (from the two upper launchers) until 700 s. The sign of the plasma currents is chosen to be positive in the direction of the total plasma current. The total ECCD is briefly 2.5 MA at 85 s, then drops to a steady state value of 0.8 MA until 400 s. The peaks caused by the upper launchers (Ant 4 and Ant 5) are near the q = 1.5 and 2.0 surfaces, simulating NTM control.

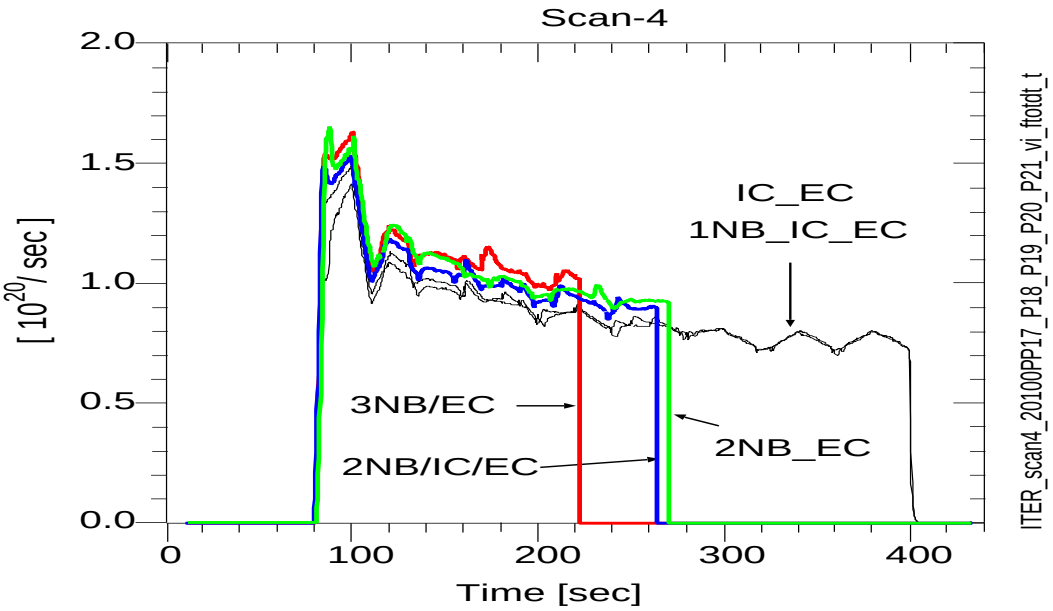

FIG. 11: Neutron emission predictions for the five heating mixes with assumptions of Scan-4. The heating mixes with two or three NNBI have broader heating profiles and lower GLF23-predicted χ_i near the mid-radius, producing higher T_i and $P_{\rm DT}$ thus producing too high $n_{\rm ash}(0)$ to maintain charge neutrality given the assumed $n_e(0)$. The assumptions of fixed $D_{\rm ash}$ and $V_{\rm ash}$, constant in radius, are unrealistic and in reality they are expected to adjust with the plasma profiles.

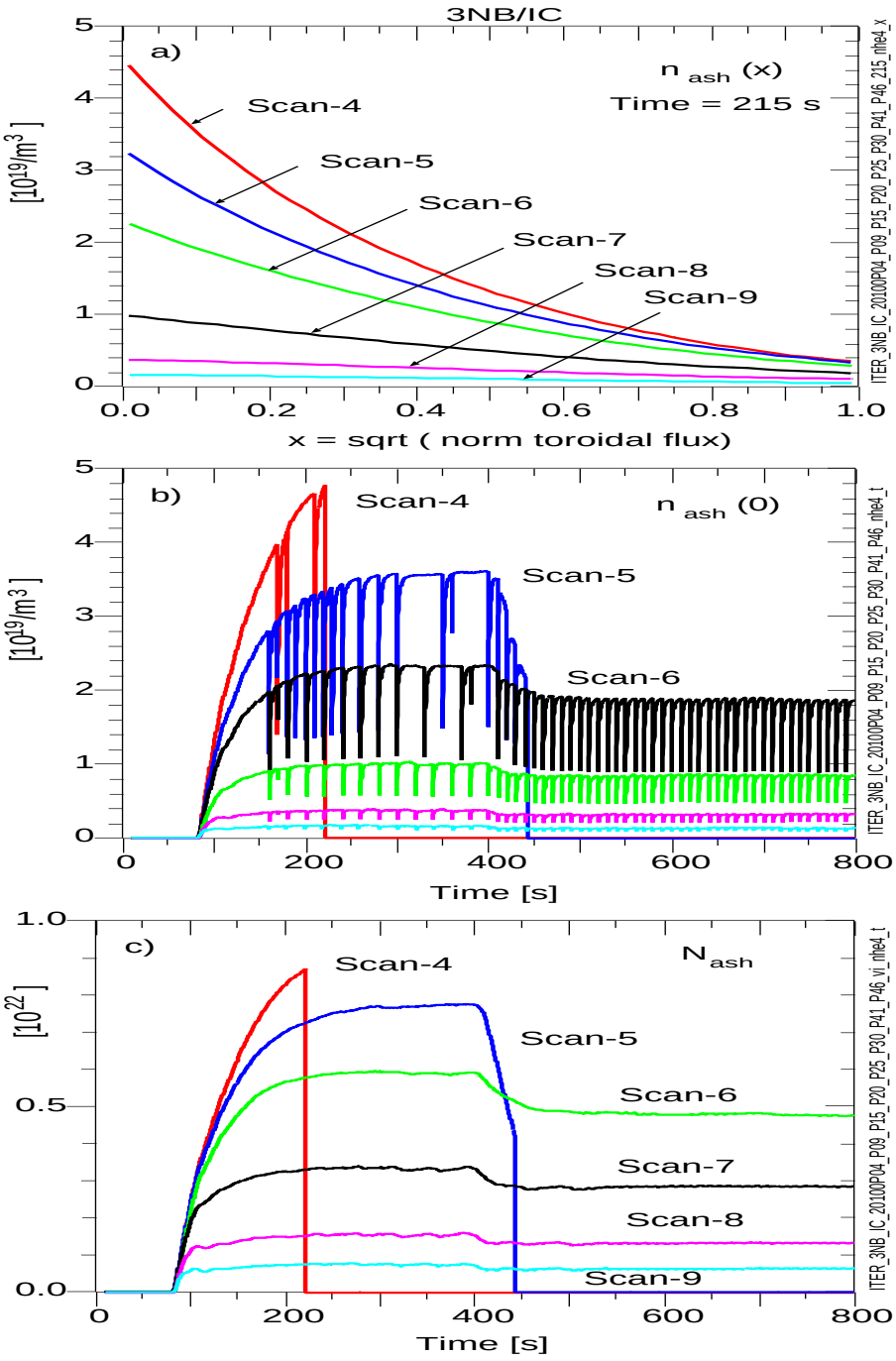

FIG. 12: Ash density profiles and time evolutions for the heating mix 3NB/IC and assumptions of Scans 4-9. The time shown is close to the time when the 3NB/EC heating mix crashes, as shown in Fig. 11.

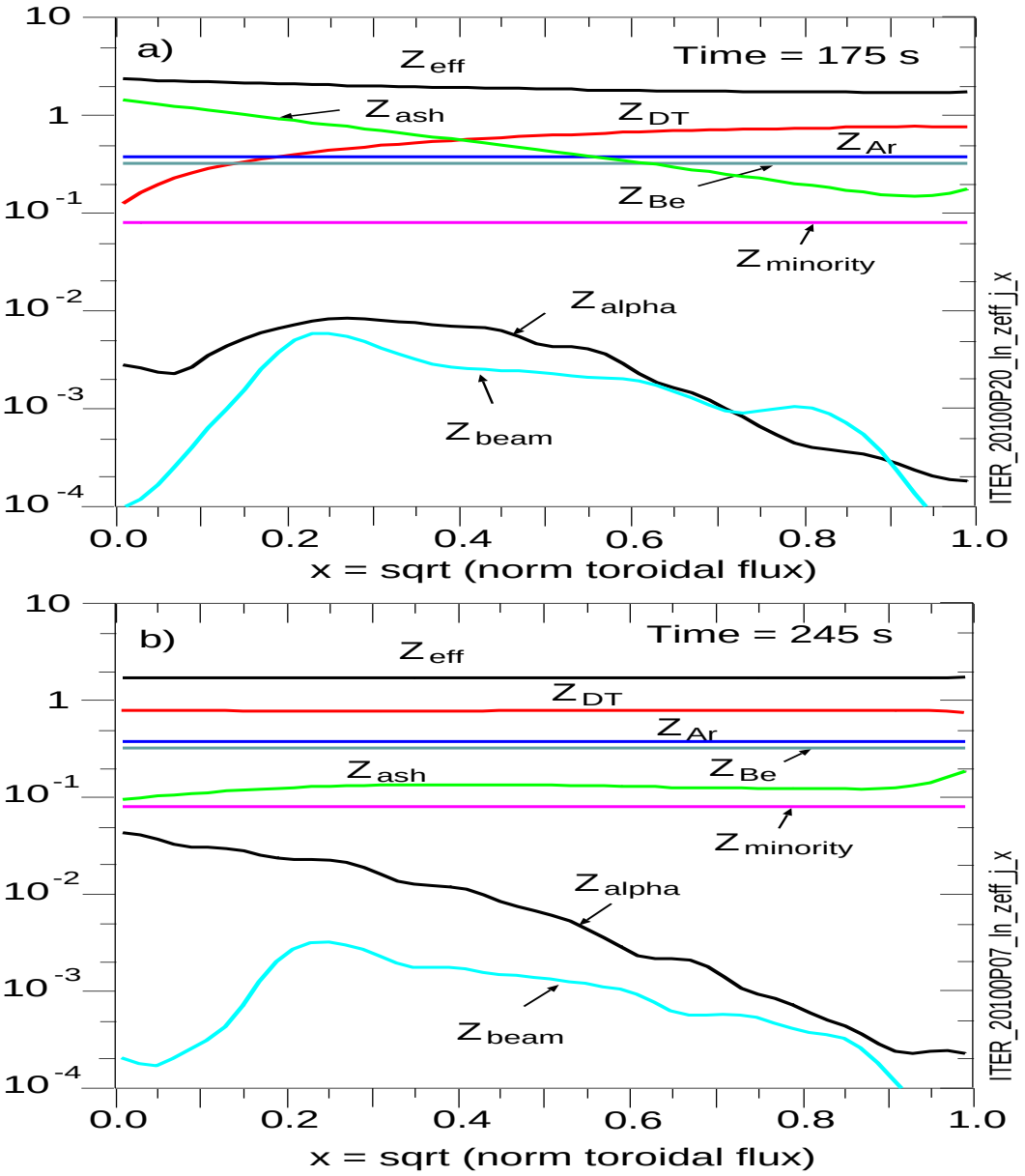

FIG. 13: Profiles of contributions to Z_{eff} for a) heating mix 3NB/IC with assumptions of Scan-4, and b) heating mix 2NB/IC/EC with assumptions of Scan-2. The time 175 s chosen for a) is before the crash of the 3NB/EC heating mix, as shown in Fig. 11. The total Z_{eff} is approximately 2.4 in the core and 1.75 at the pedestal. The dominant contributions in the core are from the impurities. In b) the total Z_{eff} is approximately 1.72. The dominant contributions are from the DT, and from the Ar and Be impurities. In both cases the contributions from the ^{3}He minority, fast alpha, and beam ions are relatively small.

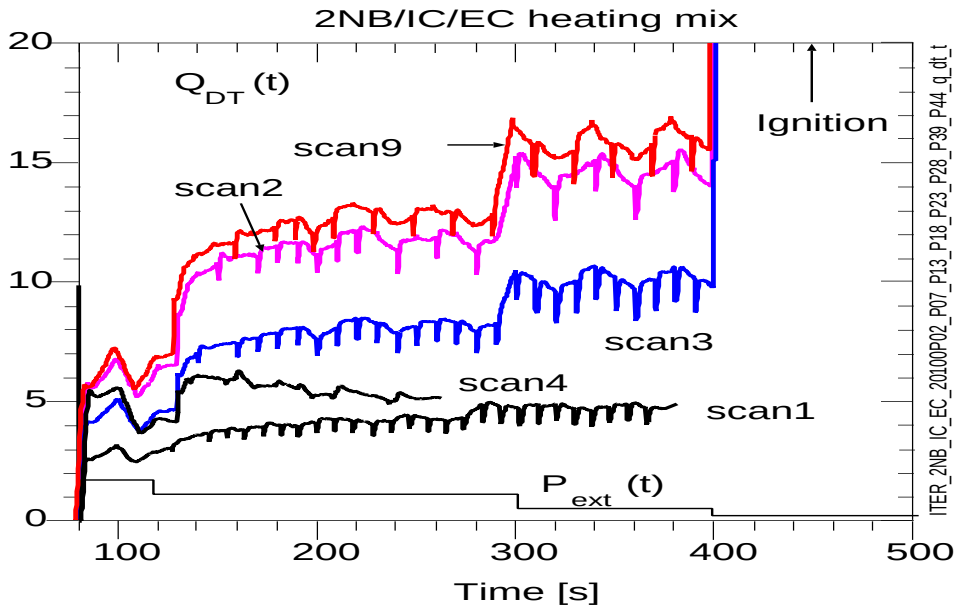

FIG. 14: Q_{DT} versus time for scans with heating mix 2NB/IC/EC.

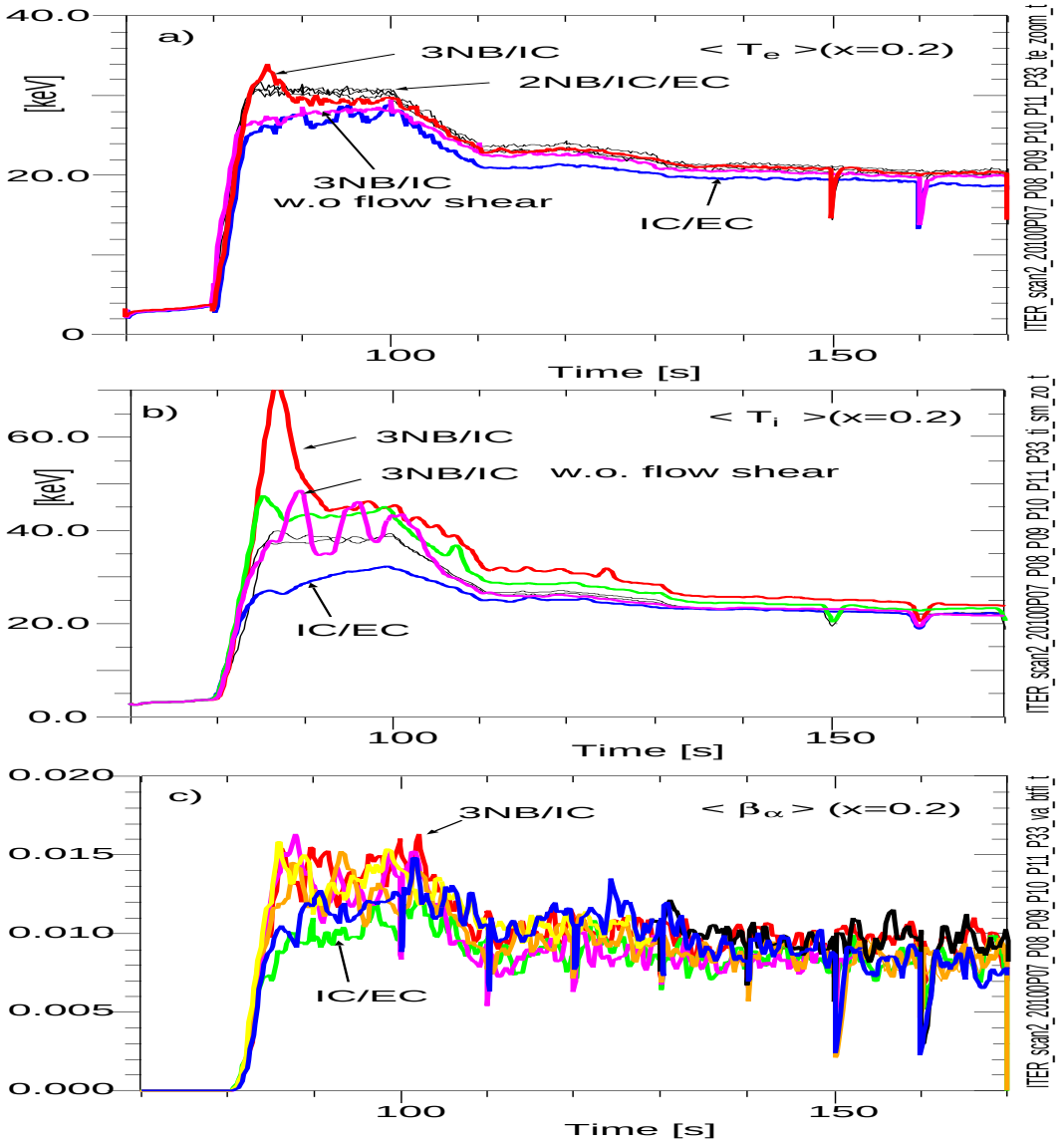

FIG. 15: Central temperatures and β_α during the early heating phase for physics Scan-2. The profiles are volume-averaged to x=0.2 to reduce sawtooth effects. Scans with three NNBI sources (mix 3NB/IC) are predicted to have relatively high ion temperatures (as observed in supershots and Hot-ion H-mode plasmas). Effects of flow shear suppression is illustrated in a)and b) for the heating assumption 3NB/IC by comparing predictions with out flow shear. The peak values of β_α are more than twice the peak values of the similarly-defined β_{beam} which decrease rapidly after 100 s.

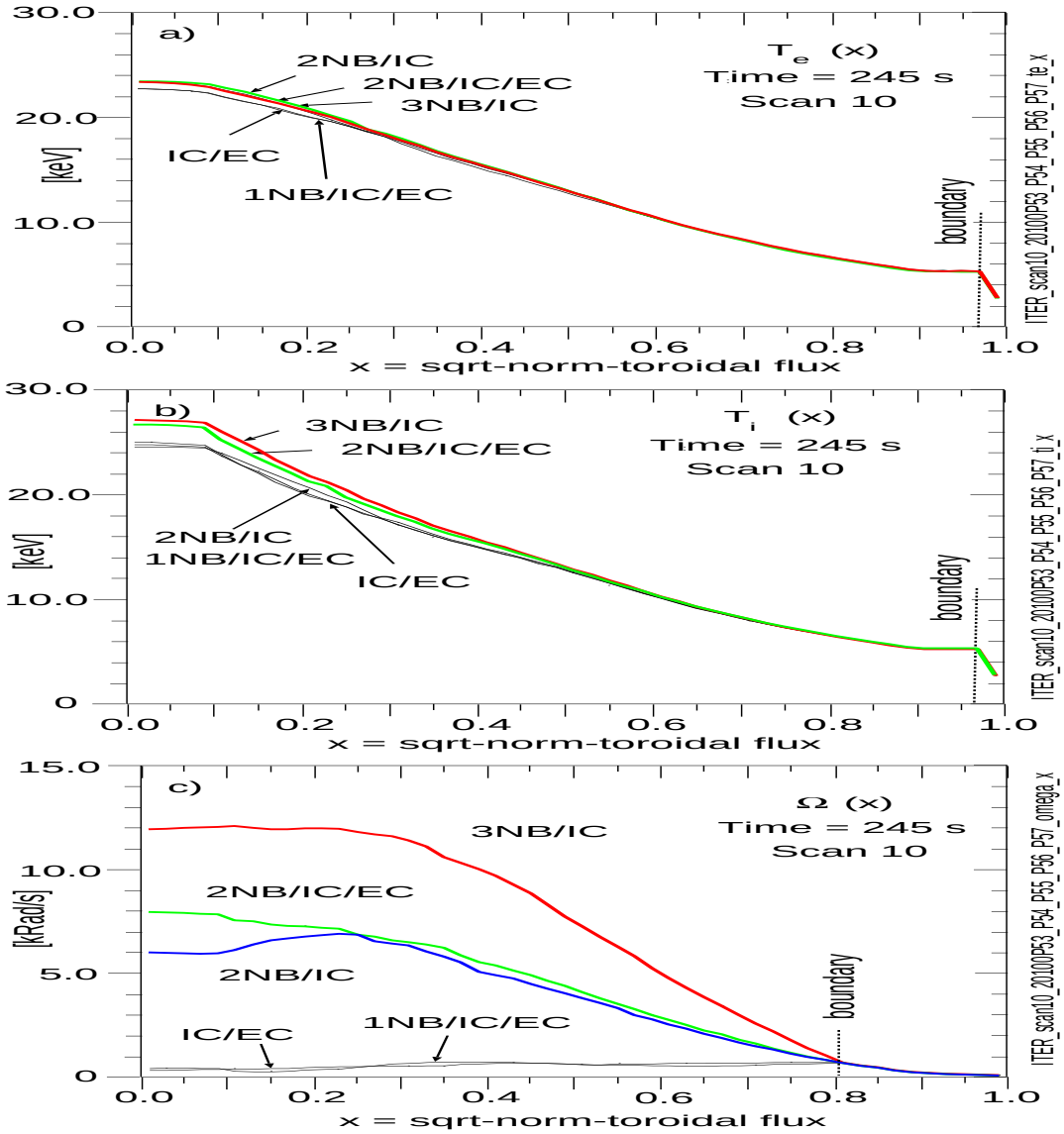

FIG. 16: Plasma profiles at a steady state time between sawteeth for the five heating mixes with the physics assumptions of Scan-10. The boundary location is from the PEDESTAL model in PTRANSP, and the boundary temperatures are scaled up a factor of 1.8 from those of the PEDESTAL model. The toroidal rotation is computed from $\chi_\phi/\chi_i = 0.5$, NNBI torque, and boundary set by an assumed profile past x=0.8. The Mach number (ratio of average thermal velocity and thermal sound speed) of the 3NB/IC mix is 0.085 for the bulk D and T ions. The range of $P_{\rm DT}$ is 472-533 MW during the steady state phase 250-400s

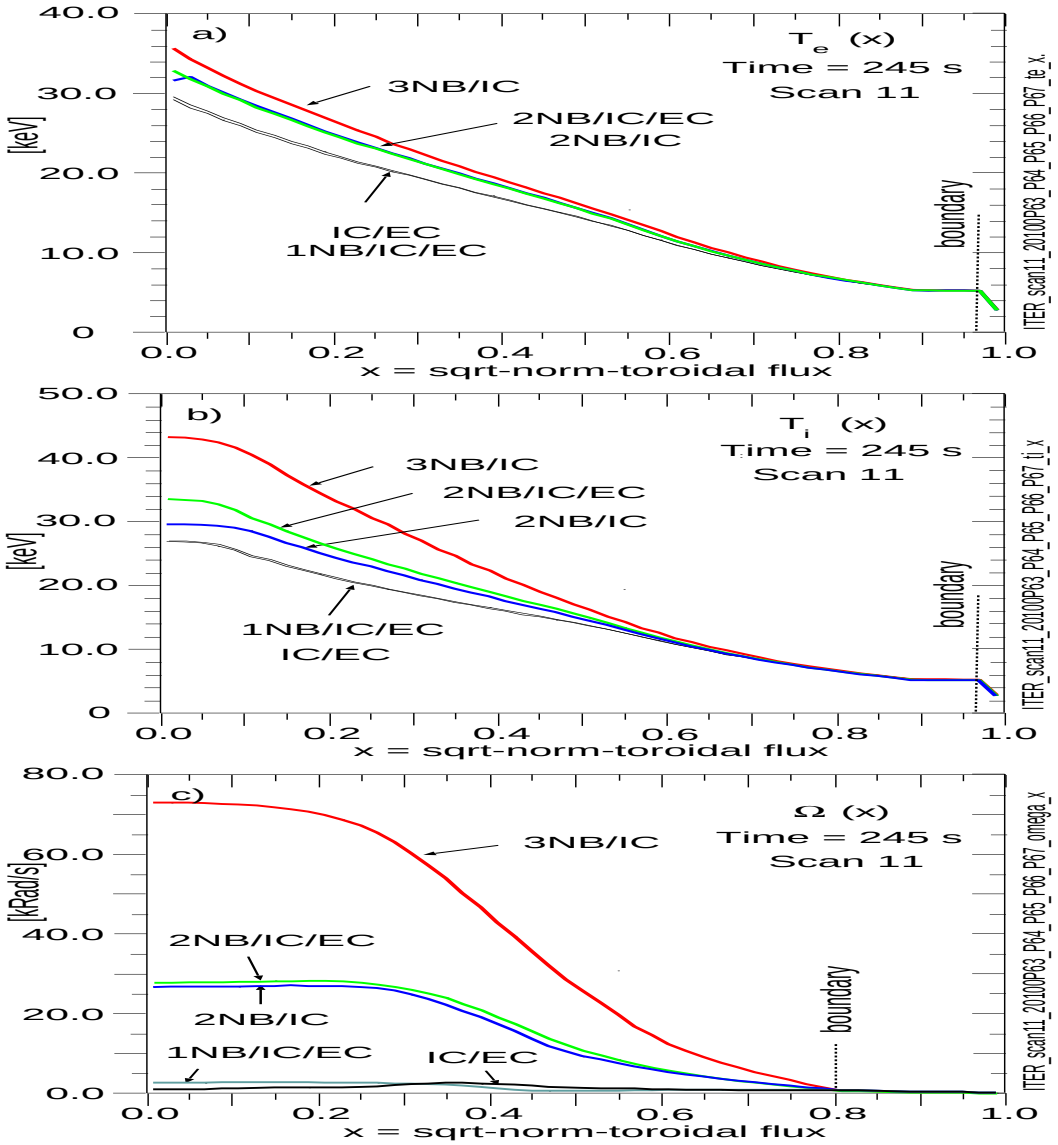

FIG. 17: Plasma profiles at a steady state time between sawteeth for the five heating mixes with the physics assumptions of Scan-11. The boundary location is from the PEDESTAL model in PTRANSP, and the boundary temperatures are scaled up a factor of 1.8 from those of the PEDESTAL model. The toroidal rotation is computed from GLF23, NNBI torque, and boundary set by an assumed profile past x=0.8. Even with no torque (mix IC/EC) there is a non-zero v_{tor} from the boundary, and significant flow shear effects on T_e. The Mach number (ratio of average thermal velocity and thermal sound speed) of the 3NB/IC mix is 0.4 for the bulk D and T ions. The range of $P_{\rm DT}$ is 528-703 MW during the steady state phase 250-400s

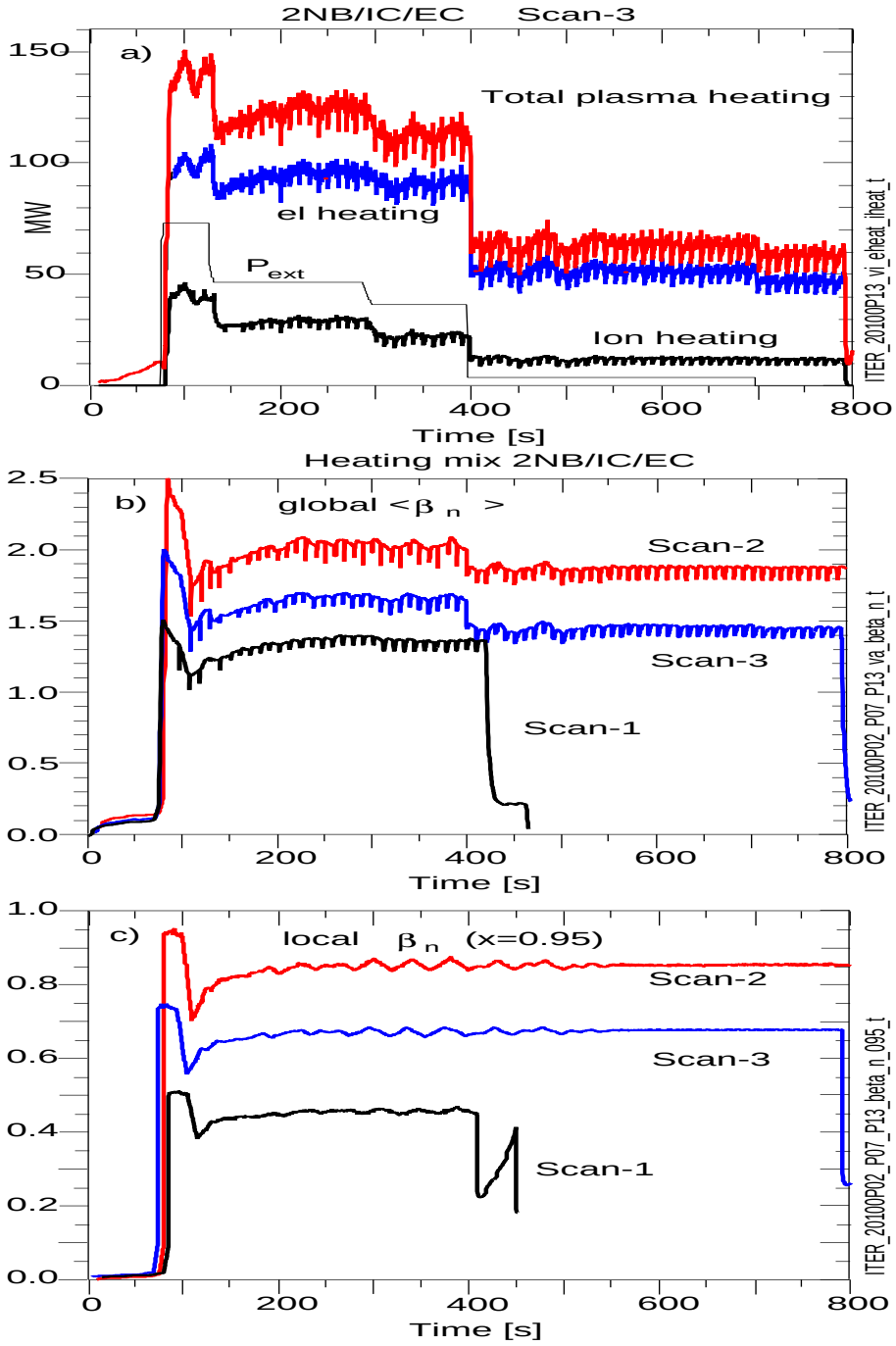

FIG. 18: a) Heating powers vs time for one of the Scan-2 predictions; b) Global $< \beta_n >$; and c) Local $\beta_{n,ped}$ versus time for three predictions.

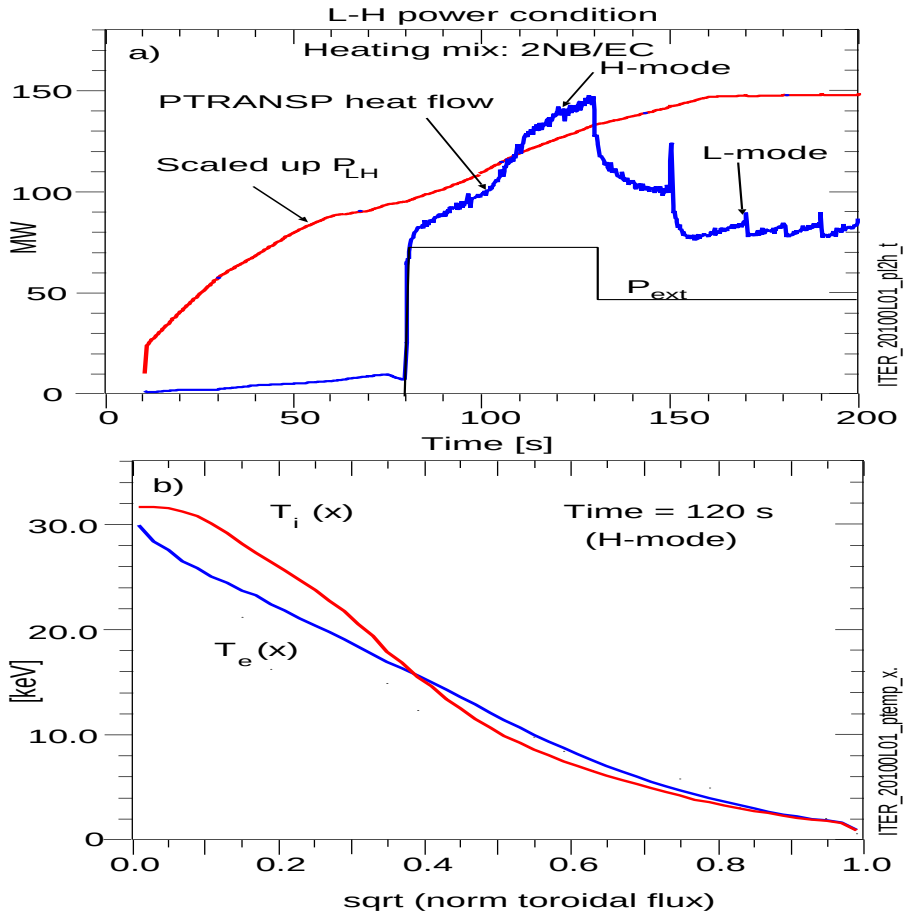

FIG. 19: a) Comparison of the heating power required for the H-mode transition (from PEDESTAL, scaled up a factor of three) with the total heating and $P_{\rm ext}$; b) GLF23-predicted temperatures during a time in the H-mode phase assuming $T_{\rm ped}$ from PEDESTAL scaled down by a factor of 0.8.

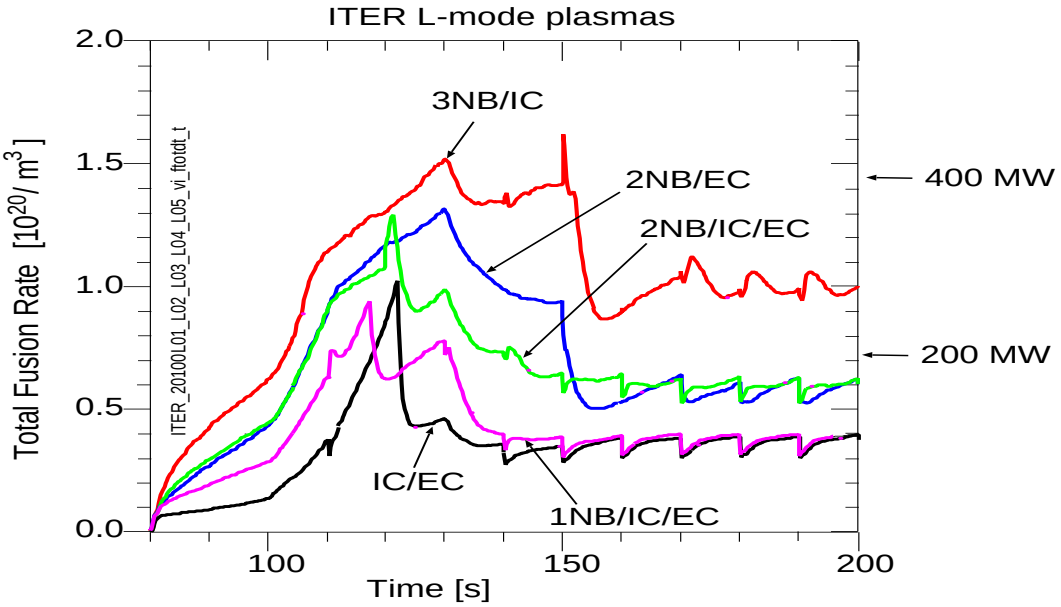

FIG. 20: Neutron emission and $P_{\rm DT}$ from L-mode plasmas with various heating mixes. Effects of sawtooth mixing are seen.

The Princeton Plasma Physics Laboratory is operated
by Princeton University under contract
with the U.S. Department of Energy.

Information Services
Princeton Plasma Physics Laboratory
P.O. Box 451
Princeton, NJ 08543

Phone: 609-243-2750
Fax: 609-243-2751
e-mail: pppl_info@pppl.gov
Internet Address: http://www.pppl.gov